PONTIFICIA UNIVERSIDAD CATÓLICA DE CHILE
INSTITUTE OF ASTROPHYSICS

CHARACTERIZATION OF THE DWARF GALAXY POPULATION IN THE CENTAURUS A ENVIRONMENT

KAREN X. RIBBECK

A thesis submitted to the Institute of Astrophysics of Pontificia Universidad Católica de Chile for the degree of MSc in Astrophysics

Supervisor	:	Dr. Thomas Puzia
Corrector	:	Dr. Gaspar Galaz
Corrector	:	Dr. Felipe Barrientos

November 2020
Santiago, Chile

ABSTRACT

We report photometric properties of the dwarf galaxy population in the Centaurus A group, along with 51 new dwarf candidates based on the optical $u'g'r'i'z'$ imaging of 22 deg^2 centered on the nearby giant elliptical galaxy NGC 5128 as part of The Survey of Centaurus A's Baryonic Structures (SCABS) program. Morphological analysis of the new candidates shows surface brightness profiles are well represented by a single component Sérsic models with an average Sérsic index of $\langle n \rangle = 0.85 \pm 0.05$. The candidates present luminosities of $-12 \lesssim M_V \lesssim -7$ mag, corresponding to stellar masses of $7.5 \gtrsim \log \mathcal{M}_*/M_\odot \gtrsim 4.5$, which extend the size-luminosity relation toward fainter luminosities and smaller sizes for known dwarf galaxies outside the Local Group (LG), and are consistent with properties of nearby dwarf spheroidal galaxies. I will discuss the stellar population properties of the newly discovered galaxy sample and compare their properties to other dwarf galaxy samples in the nearby Universe.

ACKNOWLEDGMENTS

I would first like to thank my thesis advisor Dr. Thomas H. Puzia, for all the help and support during the entire process of the master's degree. Thank you for all the advice, and for pushing me to accomplish this goal with new ideas and your constant enthusiasm for science.

In addition, I would also like to express my very special appreciation for my research group members, for always listening to me, and providing helpful remarks and ideas about my work, special thanks to Paul, Matt, Yasna, and Linda, who actively helped me with the detection process at the beginning of the thesis.

I could not leave out a very special thanks to my friends, especially Lupe, Pia, Lery and Juan, who have always been there for me, supporting me and encouraging me at all times, and lending their shoulder when things seemed difficult.

Finally, I must express my most profound gratitude to my family, my parents Ximena and Pablo, to whom I not only owe my life but also everything I have come to be. Also my siblings Klaus and Kurt, and to my boyfriend Cris for providing me with unfailing support and continuous encouragement throughout my years of study and through the process of researching and writing this thesis. This accomplishment would not have been possible without them. Thank you.

CONTENTS

LIST OF FIGURES

LIST OF TABLES

Part I

INTRODUCTION

1 INTRODUCTION

1.1 Λ+COLD DARK MATTER

A Universe dominated by dark energy and Cold Dark Matter, with a small component of baryons (Planck Collaboration et al. [52]) is consistent with observations on large scales, from the horizon (~ 15.000 Mpc) to the typical spacing between galaxies (~ 1 Mpc), and its evolution with time. The ΛCDM cosmological model is also successful at explaining the basic properties of galaxies that form within dark matter halos, hydrodynamical simulations of galaxy formation are capable of reproducing a large variety of galaxy luminosities, sizes, colours, morphologies and evolutionary stages, providing a powerful tool for galaxy formation theories (Vogelsberger et al. [62], Schaye et al. [54]).

However, when the first N-body simulations resolved the internal structure of CDM halos on small scales, length scales smaller than ~ 1 Mpc and mass scales smaller than $\sim 10^{11} M_{\odot}$, the ΛCDM model presented tensions with observations, some of these challenges are:

1. Missing Satellites

   High-resolution cosmological simulations of Milky Way sized dark matter halos in the ΛCDM paradigm have demonstrated that dark matter clumps exist at all resolved masses, with no break in the subhalo mass function down to the numerical convergence limit (e.g., Springel et al. [57]). While thousands of subhalos are expected, only ~ 60 satellite galaxies are known to orbit within the virial radius of the Milky Way.

   The observed stellar mass function of field galaxies and satellite galaxies in the Local Group is much flatter at low masses than the predicted dark matter halo mass functions: $dn/dM_* \propto M_*^{\alpha_g}$ with $\alpha_g \simeq -1.5$, compared to $\alpha_{dm} \approx -2$ for dark matter (Moore et al. [40], Jenkins et al. [23]).

   Either ΛCDM predictions are not reliable, or there are many dwarfs galaxies not yet discovered. One solution to this problem is to expect that galaxy formation become increasingly inefficient as the halo mass drops, making it impossible for the smallest dark matter halos to form stars. Another solution is take into account various baryonic effects, like the impact of reionization which results in predictions that are in rather good agreement with observations (Bullock, Kravtsov, and Weinberg [11]).

2. Cusp/Core

   The central regions of dark-matter dominated galaxies tend to be both less dense and less cuspy than predicted for standard ΛCDM halos.

   Numerical simulations that include only dark matter predict that dark matter halos should have density profiles that rise steeply towards the centers of galaxies, being described as $\rho \propto r^{\gamma}$, with $\gamma \approx -1$ (e.g., Moore et al. [39], Navarro et al. [47]). This profile is in contrast with many low-mass dark-matter-dominated galaxies with well-measured rotation curves which prefer dark matter halos with constant-density cores ($\gamma \approx 0 - 0.5$, e.g. McGaugh, Rubin, and de Blok [37]).

   A related issue, referred to as "central density problem", where ΛCDM model predicts excessively high dark matter densities in the central parts of halos (Alam, Bullock, and Weinberg [1]).

3. Too-Big-To-Fail

   A solution to the missing satellites problem within ΛCDM is to assign the known Milky Way satellites to the largest dark matter subhalos, and attribute the lack of observed galaxies in the remaining smaller subhalos to galaxy formation physics. Boylan-Kolchin, Bullock, and Kaplinghat [9] suggest that the inferred central masses of Milky Way satellites should be consistent with the central masses of the most massive ΛCDM simulations of Milky Way-mass halos. Contrary to this prediction, subhalos with masses comparable to Milky Way satellites are not among the most massive satellites predicted by ΛCDM, the most massive satellites would be "too big to fail" to form galaxies if the lower-mass satellites are capable of doing so.

4. Satellite Planes

   Satellite galaxies appear to align on a polar great circle around the Milky Way (e.g. Kunkel and Demers [31], Lynden-Bell [33]). Kroupa, Theis, and Boily [30] argued the anisotropic distribution of Milky Way satellites is inconsistent with them being drawn from a cosmological sub-structure population, therefore cannot be related to dark-matter dominated satellites. 3D motions of MW satellites suggest there is a preferred orbital pole aligned perpendicular to the observed planar plane (Pawlowski and Kroupa [50]). Orbital poles and MW spatial configuration are highly unusual for a randomly drawn sample of ΛCDM subhalos (Pawlowski et al. [51]).

1.2 DWARF GALAXIES

The least luminous known galaxies have historically been those closest to the Milky Way, in 1999 the Local Group contained 36 known members, of which 11 are Milky Way satellites (van den Bergh [66]). A combination of theoretical results, simulations showing the discrepancy between the predicted number of dark matter halos orbiting the Milky Way and the 11 observed by that time, and the arrival of digital sky surveys have initiated a renaissance in the search and discovery rate of low-luminosity dwarf galaxies throughout the local universe at distances $\lesssim 50\ Mpc$.

During the last decade the number of dwarf galaxies in the Local Group (LG) has risen to include dozens (e.g. Belokurov et al. [4], McConnachie [36], Bechtol et al. [2], Muñoz et al. [42], Muñoz et al. [43]), and rich systems of dwarfs have been discovered beyond the Local Group, around nearby giant galaxies like M81, M101, NGC 2784, M96, and others (Chiboucas, Karachentsev, and Tully [12], Merritt, van Dokkum, and Abraham [38], Javanmardi et al. [22], Bennet et al. [5], Henkel et al. [21], Müller et al. [46], Müller, Jerjen, and Binggeli [45]), and galaxy clusters like Fornax and Virgo (Muñoz et al. [41], Sánchez-Janssen et al. [53], Eigenthaler et al. [18], Ordenes-Briceño et al. [48]).

Therefore, identifying and studying these faintest dwarf galaxies in the local universe are useful to constrain the ΛCDM model and address, for example, the missing satellite problem. A way to quantify this problem is by comparing the faint-end slope of the galaxy luminosity – described by a Schechter (1976) function of the form $\phi(M_B)dM \propto 10^{0.4(M_*-M)(\alpha+1)}dM$ – observed, with the faint-end slope $\alpha \approx -2$, predicted by ΛCDM for the mass spectrum of the cosmological dark matter halos (Moore et al. [40], Jenkins et al. [23]).

1.2.1 *Classification and Distribution*

Adopting the dwarf galaxy naming convention, the term "dwarf" refers to galaxies with $M_* \lesssim 10^9 M_\odot$, and we can subdivide dwarfs into three mass classes: Bright Dwarfs ($M_* \approx 10^{7-9} M_\odot$), Classical Dwarfs ($M_* \approx 10^{5-7} M_\odot$), and Ultra-faint Dwarfs ($M_* \approx 10^{2-5} M_\odot$).

Another common classification for dwarf galaxies is between dwarf elliptical (dE) which are elliptical in shape, contain few or no gas with no evidence of recent star formation, dwarf spheroidals (dSph) which exist at the faint end of the dwarf elliptical scale, are more ellipsoid in shape with smaller diameters, and dwarf irregulars (dIrrs), for those with gas and dust, and ongoing star formation. Note that most dSph galaxies are satellites of larger systems, and the vast majority of field dwarfs are dIrr.

Part II

DWARF GALAXY CHARACTERIZATION

2 THE DATA

2.1 OBSERVATIONS

Observations from the Survey of Centaurus A's Baryonic Structures (SCABS) were used for this work. SCABS is a wide-field, multi-band imaging campaign (Taylor et al. [58]) mapping the central volume of the Centaurus A galaxy group in the five optical u', g', r', i', and z' filters. The data were taken during the nights of 4-5 April 2014 (CNTAC ID: 2014A-0610; PI: Matthew Taylor), and 25-27 August 2014 (CNTAC ID: 2014B-0609; PI: Roberto Muñoz) using the Dark Energy Camera (DECam; Flaugher et al. [19]) mounted on the 4-meter Blanco telescope at the Cerro Tololo Inter-American Observatory (CTIO) in Chile.

SCABS uses the large field-of-view of DECam (3 deg^2 per pointing) to image NGC 5128 out to its approximate virial radius of $\sim$ 300 kpc, shown in Figure 2.1 (Taylor et al. [58]) as the red-dashed ellipse, covering $\sim$ 72 deg^2 of the sky around NGC 5128. For each pointing a five-point dithering strategy was used to cover the DECam chip gaps.

During the 2014A-0610 program images with $5 \times 240 = 1200s$, $5 \times 20 = 100s$, $5 \times 12 = 60s$, $5 \times 20 = 100s$ exposures, and $5 \times 40 = 200s$, for u', g', r', i', and z' filters, respectively. These exposure times were selected in order to reach S/N $\approx$ 5 apparent point-source depths of $m_{u'} \simeq 24.1$ mag, $m_{g'} \simeq 22.7$ mag, $m_{r'} \simeq 22.5$ mag, $m_{i'} \simeq 22.1$ mag, and $m_{z'} \simeq 21.7$ mag, able to reach the globular cluster luminosity function turn-over magnitude at the distance of 3.8 Mpc.

2.2 DATA REDUCTION

Image preprocessing was carried out by the DECam community pipeline (CP; Valdes, Gruendl, and DES Project [61]) to remove instrumental signatures (e.g. bias subtraction, flat-fielding, cross-talk correction). From the CP calibrated frames, the ASTROMATIC1 software suite (Source Extractor, hereafter SE; SCAMP; SWARP; PSFEx; Bertin and Arnouts [7]; Bertin et al. [8]; Bertin [6]) was used to register frames to a common coordinate system and account for pixel scale distortions across the DECam field of view using the 2MASS astrometric reference star catalogue (Skrutskie et al. [56]), and calibrate the photometry to the SDSS system using frames of the LSE 44 SDSS

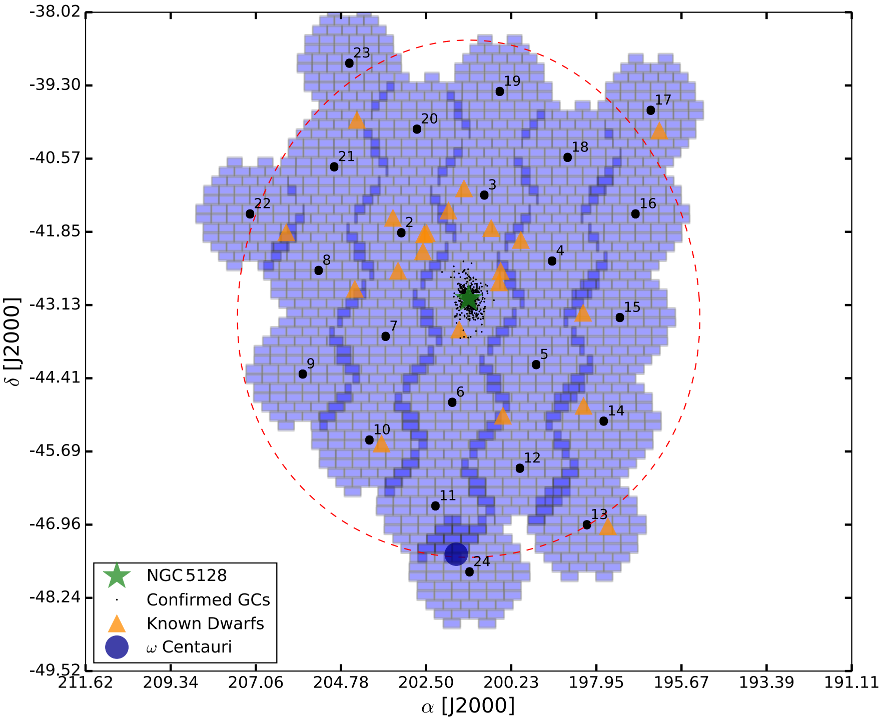

Figure 2.1: The spatial coverage of the SCABS observations. The position of NGC 5128 is shown by the green star, while the surrounding cloud of black dots indicates the population of radial velocity confirmed GCs. Orange triangles denote the positions of the previously known dwarf galaxy population within the SCABS footprint, and the position of the galactic GC ω-Centauri is indicated by the dark blue circle, which falls within the overall SCABS footprint. Different tiles are indicated by the numbers shown, with Tile1 centred on NGC 5128 itself (Fig. 1, Taylor et al. [58])

southern standard star field taken at varying airmass during the observing nights.

In the following sections an analysis of the dwarf galaxy population on Tiles 1-7 is performed, as shown in Figure 2.1.

3 DWARF DETECTION

3.1 CONFIRMED DWARFS AND KNOWN CANDIDATES IN OUR FIELD OF VIEW OF CENTAURUS A

Several dwarfs are already studied and confirmed around Centaurus A. There are 5 confirmed dwarfs on the Updated Nearby Galaxy Catalog (Karachentsev, Makarov, and Kaisina [25]), of which 1 was originally presented in Lauberts and Valentijn [32] using the ESO/Uppsala Survey of the ESO(B) Atlas, 3 in Karachentseva and Karachentsev [26] and 1 in Karachentseva and Karachentsev [27] using the POSS-II and ESO/SERC films.

Name of the galaxy, absolute B-band magnitude of galaxies corrected for Galactic and internal extinction, major linear diameter (kpc) and apparent axial ratio measured at the Holmberg isophote, and the ellipticity calculated from the latter are shown in Table 3.1.

ID	D (MPC)	A26 (KPC)	ϵ	$\langle\mu_B\rangle$ (MAG ARCSEC^2)	M_B (MAG)
KK189	4.21	0.84	0.33	25.1	−10.9
KK197	3.87	2.15	0.22	25.1	−12.9
[KK2000]55	3.94	1.09	0.12	26.4	−10.1
KK203	3.60	0.58	0.01	24.6	−10.5
ESO324-24	3.73	3.93	0.28	23.8	−15.5

Table 3.1: Photometric and Structural Parameters of Karachentsev dwarfs (Karachentsev, Makarov, and Kaisina [25]).
$A26$ is the major linear diameter in kpc, $\epsilon = 1 - b/a$

11 more dwarfs were discovered as part of the Panoramic Imaging Survey of Centaurus and Sculptor (PISCeS; Crnojević et al. [15], Crnojević et al. [16], Crnojević et al. [17]) using Megacam at the Magellan Clay 6.5m telescope, producing stacked images with a total exposure time of $5 \times 300s$ for the r'-band and $6 \times 300s$ for the g'-band reaching a 50% point source completeness limit of $r \sim 25.75$ mag and $g \sim 26.75$ mag. To quantify the structure and luminosities of the dwarf sample, Crnojević et al. work with RGB stars: dwarf centers are determined via an iterative process, computing the average of stellar positions within circles of decreasing radius; Position angle and ellipticity are measured using the method of moments for the RGB spatial distri-

ID	D (MPC)	r_{eff} (KPC)	ϵ	$\mu_{V,0}$ (MAG ARCSEC^{-2})	M_V (MAG)
Dw1	3.63	1.40 ± 0.04	0.19 ± 0.01	28.8 ± 0.1	-10.9 ± 0.3
Dw2	3.60	0.36 ± 0.08	< 0.67	28.1 ± 0.5	-8.4 ± 0.6
Dw3	4.61	2.92 ± 0.20	0.29 ± 0.19	26.7 ± 0.1	-13.0 ± 0.4
Dw4	3.91	0.35 ± 0.10	< 0.30	25.4 ± 0.7	-9.8 ± 1.1
Dw5	3.42	0.22 ± 0.04	< 0.61	26.9 ± 0.7	-7.2 ± 1.0
Dw6	3.61	0.30 ± 0.01	< 0.56	25.9 ± 0.1	-9.0 ± 0.4
Dw7	3.38	0.36 ± 0.09	0.28 ± 0.14	26.7 ± 0.9	-8.6 ± 1.3
Dw8	3.47	0.58 ± 0.05	0.26 ± 0.22	26.6 ± 0.4	-9.7 ± 0.5
Dw9	3.81	0.42 ± 0.03	0.13 ± 0.12	26.6 ± 0.3	-9.1 ± 0.4
Dw10	3.27	0.24 ± 0.06	< 0.27	26.6 ± 0.9	-7.8 ± 1.2
Dw11	3.52	0.34 ± 0.04	0.27 ± 0.21	25.8 ± 0.4	-9.4 ± 0.6

Table 3.2: Photometric and Structural Parameters of Crnojević et al. confirmed dwarfs. DW11 was first discovered in Taylor et al. [60] by the name T18-dw1318-4256.

bution; radial density profiles are calculated by counting the number of RGB stars in elliptical/circular radii and trace their radial profile. Sérsic/exponential models are fit via least squares minimization to the composite surface brightness profiles and obtain values for the effective radius and the central surface brightness, and luminosities are calculated by integrating the best-fit Sérsic/exponential profiles. Results from Crnojević et al. are presented in Table 3.2.

In Crnojević et al. [17] two of our dwarf candidates are confirmed as background galaxies. HST imaging confirmed the lack of resolved populations in these targets, excluding the possibility of them being low-mass satellites of Cen A.

There are also 8 known candidates from Müller, Jerjen, and Binggeli [44] on our field of view. Using the wide-field Dark Energy Survey camera at the 4-m Blanco Telescope at CTIO, with exposures times of $3 \times 40s$ in g' and r'-bands on the first observing run, and for the second run exposure times between 2×120 and $2 \times 210s$ for r'-band, and between 2×100 and $2 \times 170s$ for g'-band, for those relative short exposure times it is not possible to resolve galaxies at the distance of Centaurus A. To find the center of the galaxy a circle was fitted at the outer isophotes, a circular aperture was used for the photometry and Sérsic profiles were fitted to the surface brightness profiles. In this work absolute magnitudes were calculated assuming the mean distance of the Centaurus group (4.5 Mpc); their results are presented

ID	M_r (MAG)	n	$\mu_{eff,r}$ (MAG ARCSEC^{-2})	$r_{eff,r}$ (ARCSEC)
dw1318-44	-7.88	1.13 ± 0.72	26.13	4.8
dw1323-40	-11.19	1.64 ± 0.23	25.27	15.2
dw1323-40b	-10.69	1.35 ± 0.19	26.06	17.1
dw1323-40c	-10.20	2.48 ± 1.21	26.90	20.2
dw1329-45	-9.66	1.84 ± 0.27	25.86	9.9
dw1336-44	-9.74	2.45 ± 0.20	25.34	8.07
dw1337-41	-9.59	2.04 ± 0.51	27.29	18.3
dw1337-44	-9.65	1.02 ± 0.27	26.06	10.3

Table 3.3: Photometric and Structural Parameters of Müller, Jerjen, and Binggeli [44] dwarf candidates. Values are extracted from Table2 of the paper, absolute magnitudes

in Table 3.3.

In a preliminary study of SCABS's data in Taylor et al. [60], photometric properties of 16 dwarfs galaxies, 15 of which were newly identified, in the Western halo of Centaurus A are presented using the same methods as this work. All of them were found at projected distances of $\sim 100 - 225$ kpc from their giant host, with luminosities $-10.82 \leq M_V/\text{mag} \leq -7.42$ and effective radius $75 \lesssim r_{eff}/\text{pc} \lesssim 300$, using a distance modulus of 27.88 mag (3.8 Mpc Harris, Rejkuba, and Harris [20]).

3.2 DETECTION METHOD

To detect dwarf galaxy candidates a full-color RGB image was constructed from the $u'g'z'$ frames to take advantage of the best compromise for detection between the total flux captured in each passband, and preserving color information. This filter combination samples the full optical spectral energy distribution (SED), is sensitive to old, metal-poor stellar population expected of primordial dwarf galaxies, as well as young stellar populations from more recent star-formation due to the inclusion of the u'-band, as will become evident further below when we will discuss the stellar population properties of the identified sources.

We visually inspected these frames looking for low surface brightness (LSB) galaxies. This method allow us to easily identify faint, extended sources displaying smooth morphologies and flat surface

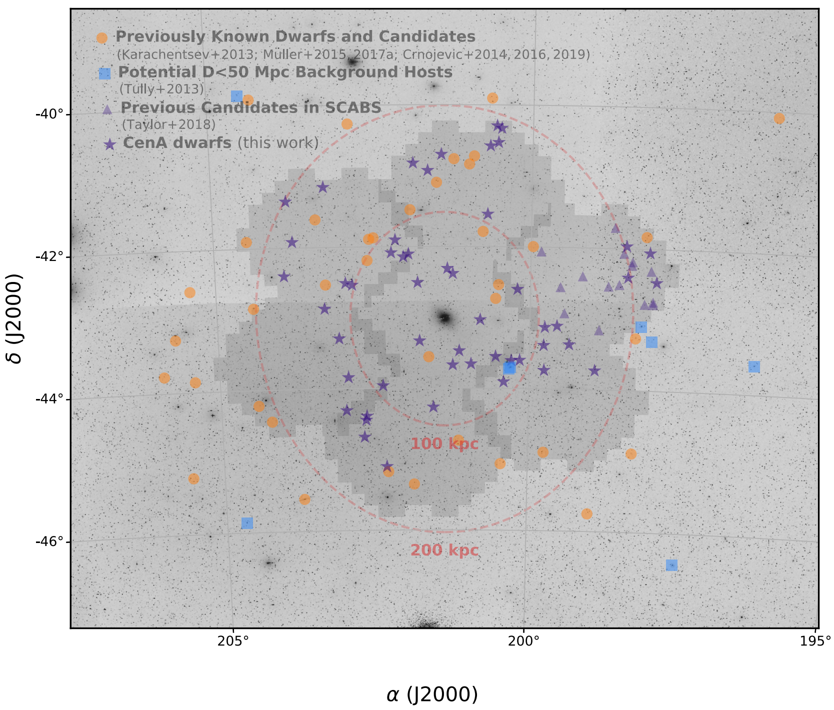

Figure 3.1: Spatial distribution of known and new dwarf galaxy/candidates on Centaurus A. Superposed on an archival DSS image is printed the footprint of the observations, orange circles indicate previously known dwarfs/candidates, while blue squares show possible background hosts. Purple stars indicate the position of the new dwarf candidates on the survey and lighter triangles those detected on a previous study of the northwest halo data.

brightness profiles, typical of low luminosity dwarf galaxies.

A by-eye classification done independently by five different persons (KXR, THP, MAT, YO, LW) was chosen above an automated algorithm because this methods, for example SExtractor, can only analyze one frame-passband at a time and often fails to detect extended LSB sources due to contamination by foreground stars, or can identify noise from image stacking as a candidate.

However, the disadvantage of visual inspection is the potential introduction of human bias and prevents us from quantifying a selection function to verify sample completeness. To decrease the human bias five different people inspected the RGB images individually, and each produced a catalog for each of the 7 different tiles.

3.2.1 *Quality Flags*

To determine which detections were reliable a flag system was chosen. We define flag A for candidates found by all five members of the search team, flag B those with four detections, and so on, until flag E being unreliable sources only detected by one of the members.

After the RGB by-eye inspection based on overall morphology, size and color, five independent detection lists for each tile are available, and a matching process is performed. A pair of coordinates (x,y) of a list is compared with every detection from all other lists, looking for distances $\lesssim 150$ pix ($\lesssim 0.73$ kpc) between the sources, we count the number of times each candidate is detected and then the coordinate is erased from the arrays. This process is repeated until all coordinates are compared.

We discovered 13 flag A candidates, 16 flag B, 36 flag C, 117 flag D, and 312 flag E, including new candidates and confirmed dwarfs/known candidates in the field. Dwarfs displayed in Table 3.1 are classified as flag A detections. However, we failed to recover some faint old known dwarfs, such as Dw1-10 shown in Table 3.2, and dwarfs in Table 3.3, except for dw1323-40 which is a flag B detection. Nevertheless, many of these galaxies were fitted using *GALFIT*, those too faint to fit are presented in Section A.2.1.

During this work only candidates flag A, B and C are considered, of which there are 51 new dwarf galaxy candidates, shown in Figure 3.1 as dark purple stars.

4 SURFACE BRIGHTNESS PROFILE MODELING

4.1 INTRODUCTION

A luminosity profile describes how the intensity (or surface brightness) $I(r)$ (or $\mu(r)$) of a galaxy varies with distance r from its center. The surface brightness of a galaxy is the amount of light per square arcsecond on the sky at a particular point in the image.

If we consider a small patch of side D in a galaxy that we view from a distance d, so that it subtend an angle α on the sky, and considering that in astronomy lengths are usually measured using the small angle formula ($\alpha_{(in\,radians)} = D/d$), we can write $I(r)$ as

$$I(r) \equiv \frac{F}{\alpha^2} = \frac{L/(4\pi d^2)}{D^2/d^2} = \frac{L}{4\pi D^2} \tag{4.1}$$

where F is the measured flux ($F = L/4\pi d^2$) and L the combined luminosity of all the stars in that region.

4.1.1 *Sérsic Luminosity Profile*

The Sérsic profile or the Sérsic's $R^{1/n}$ model is one of the most frequently used profiles to study galaxy morphology, expressed as an intensity profile,

$$I(r) = I_e\, exp\left\{ - b_n \left[\left(\frac{r}{r_e}\right)^{1/n} - 1 \right] \right\} \tag{4.2}$$

where r_e is the effective radius of the galaxy, the radius at which half of the total light of the system is emitted, and I_e is the intensity at this radius.

In magnitudes Equation 4.2 translates to

$$\mu(r) = \mu_e + \frac{2.5\, b_n}{ln(10)} \left[\left(\frac{r}{r_e}\right)^{1/n} - 1 \right] \tag{4.3}$$

where μ_e is the effective surface brightness.

Parameter b_n is chosen to ensure that r_e contains half the light

$$\int_{r=0}^{\infty} 2\pi r I(r) dr = 2 \cdot \int_{r=0}^{r_e} 2\pi r I(r) dr \tag{4.4}$$

which implies

$$\Gamma(2n) = 2\gamma(2n, b_n) \tag{4.5}$$

where $\Gamma(a)$ is the gamma function and $\gamma(a, x)$ is the incomplete gamma function. Unfortunately this equation cannot be solved analytically for b_n. In this work we have adopted the asymptotic expansion of Ciotti and Bertin [14] to $O(n^{-5})$ for $n > 0.36$

$$b_n \sim 2n - \frac{1}{3} + \frac{4}{405n} + \frac{46}{25515n^2} + \frac{131}{1148175n^3} - \frac{2194697}{30690717750n^4} + O(n^{-5}) \tag{4.6}$$

For $n \leq 0.36$ this solution diverges and instead we use a polynomial expression (fourth order) accurate to one part in 10^3 obtained by MacArthur, Courteau, and Holtzman [35]

$$b_n = 0.01945 - 0.8902n + 10.95n^2 - 19.67n^3 + 13.43n^4 \tag{4.7}$$

The parameter n is defined as the Sérsic index, and is usually referred to as a concentration parameter. When n is large, the profile has a steep inner slope and a highly extended outer wing, while when n is small the profile has a shallow inner slope and a steep truncation at large radius, as presented in Figure 4.1.

The de Vaucouleurs profile is defined with a Sérsic index of $n = 4$ and is used to describe a number of galaxy bulges, while an exponential profile ($n = 1$) is used to fit a classical galaxy disk. Due to the freedom of the Sérsic profile given by the concentration parameter n, this model is a common favourite when fitting observed luminosity profiles of galaxy samples.

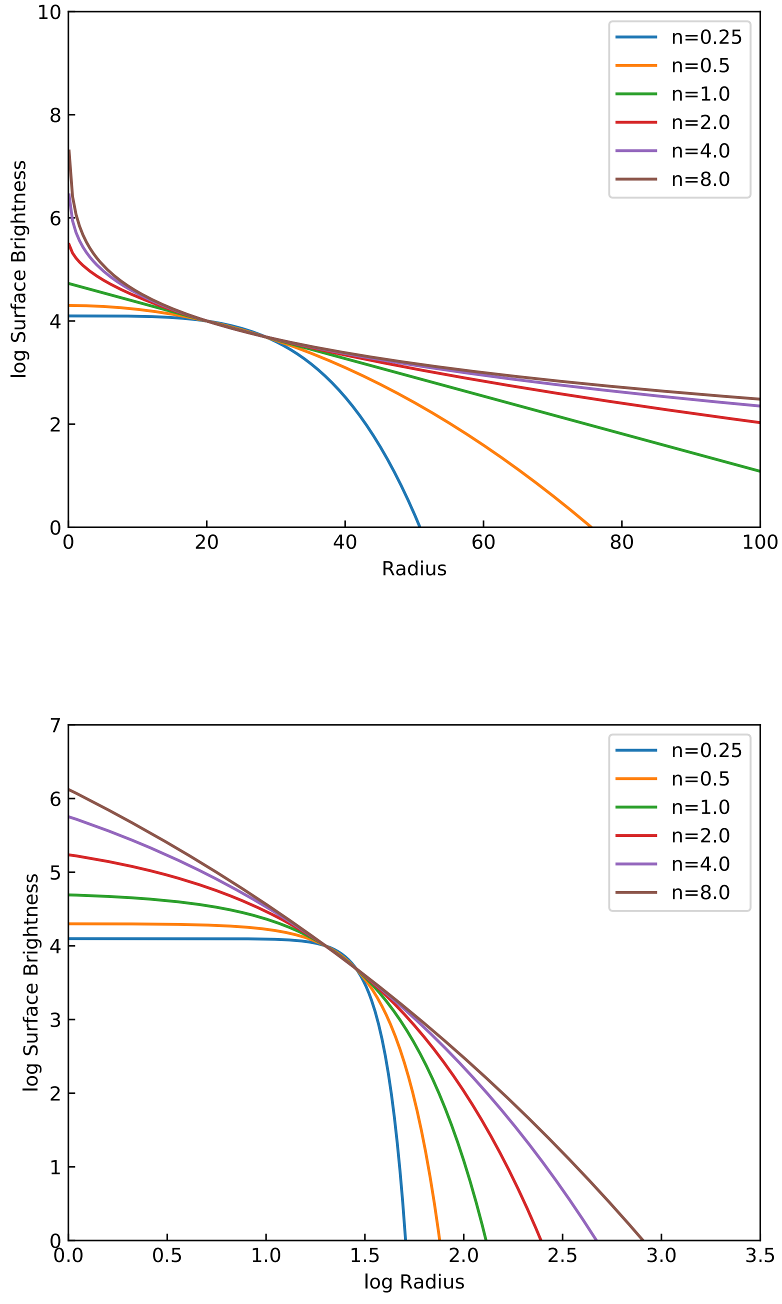

Figure 4.1: The Sérsic profile for different values of n, where r_e and I_e are held fixed. Note that for a large Sérsic index value n, the profile has a steep inner slope and a highly extended outer wing. A low n has a shallow inner slope and a more sharply truncated wing. Sérsic index values are in the range $0.25 \leq n \leq 8.0$.

4.2 GALFIT

GALFIT is a tool for extracting information about galaxies, stars, globular clusters, and other astronomical objects by using parametric functions to model objects as they appear in two-dimensional digital images. In the simplest case, it allows one to fit an ellipsoidal model, and more complicated objects with curved, irregular, ringed shapes, or have spiral arms. It is possible to mix these features within a single component model, or add them to other components for a more complex morphology.

For the functions to be useful, they generally have to have free parameters which one can adjust in order to model the desired object. If successful, the resulting features, such as luminosity, size, profile central concentration, axis ratio and position angle, are summarized and can be compared against other objects, for instance to study parameter scaling relations.

GALFIT is a least-square fitting algorithm of the non-linear type, and uses a Levenberg-Marquardt algorithm to find the optimum solution to a fit. The Levenberg-Marquardt is an iterative procedure and needs an initial guess to start the minimization. In the case with only one minimum an uninformed initial guess will work fine, otherwise, in the case of multiple minima, the algorithm will converge to the global minimum only if the initial guess is close to the final solution.

The goodness of fit is determined by calculating χ^2 and computing how to adjust the parameters for the next step. If the χ^2 decreases significantly, *GALFIT* will keep going, and when the solution no longer improves, it will stop the iteration process. The reduced χ^2 (χ^2_ν) is used as the indicator of goodness:

$$\chi^2_\nu = \frac{1}{N_{DOF}} \sum_{x=1}^{nx} \sum_{y=1}^{ny} \frac{(f_{data}(x,y) - f_{model}(x,y))^2}{\sigma(x,y)^2} \tag{4.8}$$

where N_{DOF} is the number of degrees of freedom (number of pixel - number of free parameters), nx and ny are the number of pixels on the x and y axis. The input data, $f_{data}(x,y)$, is the observed image. The model image, $f_{model}(x,y)$, is computed by *GALFIT* as it tries to find the best match to the data, and $\sigma(x,y)$ is the sigma or weight image (one standard deviation of counts at each pixel) which can be internally calculated by *GALFIT* using Poisson statistics of the data.

4.3 DWARF MODELING

Previous to modeling, cut-outs for all the 51 new candidates and confirmed dwarfs/known candidates in Cen A were created in $u'g'r'i'z'$ frames. Segmentation maps using SExtractor were constructed to create bad-pixel masks for each dwarf, resulting in dwarf-only images to fit. PSFEx software is used to obtain PSF images of the field.

For a first iteration, five different initial guesses for Sérsic model parameters (integrated magnitude, effective radius, Sérsic index, along with axis ratio and position angle) were chosen. $GALFIT$ produced a model for each initial guess for every frame ($u'g'r'i'z'$) of each dwarf. By comparison between the different models of each dwarf, we obtain a qualitative estimate of the robustness of a fit.

In the best scenario, all models converge to the same solution, but in most cases, only a couple solutions converge, and if higher contamination of other objects or the diffuse/faint nature of the dwarf is more significant, $GALFIT$ is unable to fit the galaxy, and none of the solutions converge. Galaxy, model, and residual images are inspected to assess the reliability of the fits. In most cases when the same solution is reached more than once visual inspection shows the fits to be reliable.

For a second iteration, we first consider those galaxies for which the models converge to a solution in at least one filter. For most dwarfs a reliable solution was reached in at least two or three filters, usually with the u'-band being the fainter and therefore the harder for $GALFIT$ to fit. In these cases, we fix the shape of the dwarf to obtain an estimate of the luminosity of the missing passbands. If $GALFIT$ does not converge to a solution on the first iteration, SExtractor is used to get a first estimate of the galaxy luminosity.

Once an initial luminosity guess is obtained, all parameters are set free for $GALFIT$ to try to converge to a solution. If it diverges, the luminosity is fixed to reduce the number of free parameters available for the next model, stabilizing the fit and resulting in more robust estimates of the remaining parameters. The resulting parameters are fixed to allow $GALFIT$ to recalculate luminosity freely. On the final step, luminosity is again fixed, and the other parameters are set free for one more step of optimization. Improvements to the mask images are made for better solutions.

Galaxy, model, and residual images are compared to check the reliability of the fits, leaving little to no galaxy's light on the residual image.

In the case of nucleated dwarfs, *GALFIT* is unable to fit the nuclei properly due to its small size with only one Sérsic component. Therefore we mask the nuclei and fit a single Sérsic model to the diffuse spheroid. If the nuclei is not masked correctly, *GALFIT* will attempt to fit it partially, resulting in a higher concentration parameter n, with regions of over- and under-subtraction in the residual image, clearly indicating that the nuclei have to be treated separately from the spheroid components. We present one nucleated dwarf galaxy in the sample (SCABS133523-412043).

In Appendix A figures show $u'g'r'i'z'$ frames modeling process for every dwarf, presenting galaxy, model, and residual images.

5 RESULTS

51 new dwarf galaxy candidates in Centaurus A were modeled in $u'g'r'i'z'$ frames with *GALFIT* software using a single Sérsic component, along with other confirmed dwarfs/known candidates in the field of the survey. Integrated magnitude (m), effective radius (r_e), Sérsic index (n), ellipticity (ϵ), and position angle (PA) are obtained.

Foreground extinction towards Centaurus A group is taken into account by utilizing average extinction coefficients ($A_{u'} \simeq 0.423$ mag, $A_{g'} \simeq 0.332$ mag, $A_{r'} \simeq 0.229$ mag, $A_{i'} \simeq 0.171$ mag, and $A_{z'} \simeq 0.127$ mag) calculated from several bright galaxies in the observed region, based on the re-calibrated extinction maps of Schlafly and Finkbeiner [55], in a field with extinction variance of $\sigma_{u'} \simeq 0.008$, $\sigma_{g'} \simeq 0.005$, $\sigma_{r'} \simeq 0.002$, $\sigma_{i'} \simeq 0.001$, and $\sigma_{z'} \simeq 0.001$. During this work we adopt a distance modulus of 27.88 (3.8 Mpc, Harris, Rejkuba, and Harris [20]), corresponding to a spatial scale of 18.42 pc arcsec^{-1}.

5.1 STRUCTURAL PARAMETERS

The upper panels in Figure 5.1 compare structural parameters of the entire galaxy sample, and lower panels show the distribution of structural parameters in different bands. Shown results are available in Table B.2.

If we assume the galaxies to be homologous in all passbands, a unity line would be expected when comparing different passbands, and the observed scatter would arise only from statistical uncertainties of the measurement. Although, color gradients also play a role in the scatter, having u'-band more sensitive to recent SF, while NIR colors have a stronger sensitivity to metallicity.

R^2 values were computed to compare different bands. In general, i' vs. u'-band scatter is systematically bigger compared to other bands, in part due to the shallower u'-band images, and color gradients. R^2 values also show tighter correlations for r_e and PA, being these parameters the best to constrain galaxy models. On the other hand, n and ϵ present a greater scatter, that could be due to star/gas distribution within the galaxy.

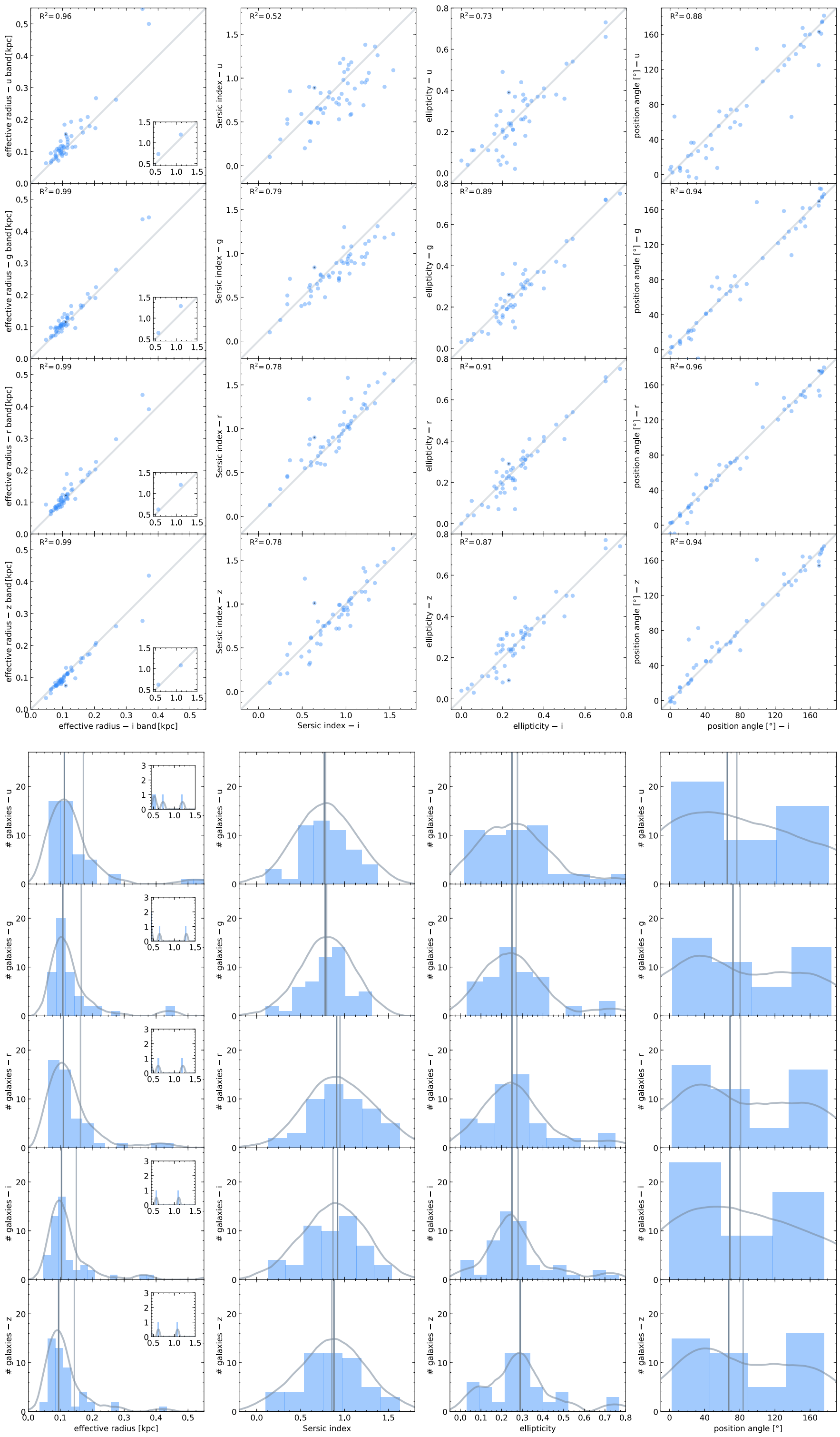

Figure 5.1: Structural parameter derived from *GALFIT* in the u', g', r', i', and z' filters. Upper panels: Comparison of effective radius (r_e), Sérsic index (n), ellipticity (ϵ), and position angle (PA) i'-band values with four other bands. Corresponding R^2 values for fitted unity line are shown on upper left corner of each figure. Lower panels: structural parameter distribution in all passbands. Smooth curve shows Epanechnikov-kernel probability density estimates for the entire sample, and vertical lines indicate the mean (light) and median (dark) of the overall distribution of entire sample.

Lower panels show distributions of r_e, n, ϵ, and PA of every passband. The histogram number of bins for each data set were chosen using Knuth's rule (Knuth [29]), non-parametric Epanechnikov-kernel probability density estimates (KDEs) are shown as solid lines for each parameter-filter combination, and vertical lines show the mean (dark) and median (light) of the data.

Well-defined peaks can be seen for r_e and n distributions. The effective radius r_e is distributed between $0.05 \lesssim r_e/\mathrm{kpc} \lesssim 1.18$, with similar average values $\langle r_e \rangle_{u'} = 0.17 \pm 0.03$ kpc, $\langle r_e \rangle_{g'} = 0.17 \pm 0.03$ kpc, $\langle r_e \rangle_{r'} = 0.16 \pm 0.02$ kpc, $\langle r_e \rangle_{i'} = 0.15 \pm 0.02$ kpc, and $\langle r_e \rangle_{z'} = 0.14 \pm 0.02$ kpc. Distribution functions show that most of our sample is concentrated near average values, with 96% of the dwarf sample exhibiting $r_e < 0.5$kpc. Such compact fluffly objects could belong to a giant host galaxy cluster in the background.

Morphological analysis of the new candidates shows surface brightness profiles are well represented by a single component Sérsic model with an average Sérsic index of $\langle n \rangle_{u'} = 0.78 \pm 0.04$, $\langle n \rangle_{g'} = 0.80 \pm 0.04$, $\langle n \rangle_{r'} = 0.95 \pm 0.05$, $\langle n \rangle_{i'} = 0.87 \pm 0.04$, and $\langle n \rangle_{z'} = 0.86 \pm 0.05$, similar to exponential profiles.

Ellipticity and position angle are more broadly distributed in all different passbands. 94% of our dwarf candidate sample present $\epsilon < 0.55$ with a similar $\langle \epsilon \rangle$ in every filter. However, we note there may be an observational bias in n and ϵ, due to the search of spheroidal diffuse objects. PA distribution show a lack of horizontal align objects, only 17% of the candidates show $60 < PA < 120$.

5.2 STELLAR MASSES

To study scaling relations and compare properties of our dwarf sample with other astronomical objects, stellar masses were calculated using the prescription from Bell et al. [3] using color-derived mass-to-light ratios.

$$log(\mathcal{M}_*/L)_\odot = a_\lambda + (b_\lambda \times color) \tag{5.1}$$

where ($\mathcal{M}_*$/L) is in solar units, and coefficient a_λ and b_λ are available for $g'r'i'z'$ bands (Bell et al. [3], Table 7).

We derived galaxy luminosity for $g'r'i'z'$ bands

$$L = 10^{-0.4(M-M_\odot)} L_\odot \tag{5.2}$$

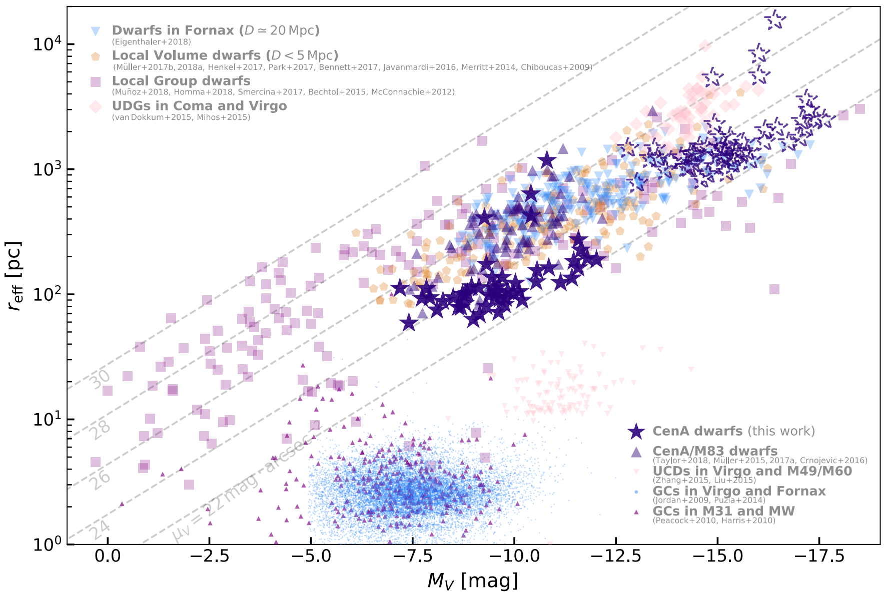

Figure 5.2: Size-Luminosity diagram displaying present dwarf galaxy candidates in Centaurus A, compared to other nearby dwarfs and other stellar systems (see legend). Dotted lines present iso-surface brightness, μ, (mag arcsec^{-2}). Empty dashed stars show this work galaxy sample shifted to a distance of 50 Mpc.

using absolute solar magnitudes ($M_\odot$) measured by Willmer [63]. We use measured and de-reddened $(u' - g')_0$, $(u' - r')_0$, $(u' - i')_0$, $(u' - z')_0$, $(g' - r')_0$, $(g' - i')_0$, $(g' - z')_0$, $(r' - i')_0$, and $(r' - z')_0$ galaxy colors, yielding up to 36 estimates of $\mathcal{M}_*$ for each galaxy, we adopt the average of individual estimates as the measured $\mathcal{M}_*$ and its error as one standard deviation of the sample. The galaxy sample has an average stellar mass of $\log \langle \mathcal{M}_* \rangle = 6.38 \pm 0.07$, spanning in the range $4.8 \lesssim \log \mathcal{M}_*/M_\odot \lesssim 7.7$.

5.3 SCALING RELATIONS

Figure 5.2 shows the effective radius (r_e, in parsec) as a function of M_V, and in Figure 5.3 as a function of stellar mass ($\mathcal{M}_*$, in solar units) for the new SCABS dwarf candidates. We compare our data (dark purple stars) to confirmed dwarfs and known candidates in the Centaurus A/M83 complex, as well as other dwarfs from the literature and other low-mass stellar systems (UDGs, UCDs, and GCs). Iso-surface brightness (μ, mag arcsec^{-2}) lines, and iso-stellar mass surface density ($\sum_{eff,M_*}$, $M_\odot pc^{-2}$) lines are shown, respectively.

M_V values were converted from g' and r'-band photometry using Jester et al. [24] transformation

$$V = g - 0.58(g - r) - 0.01 \tag{5.3}$$

For literature values M_V is converted from g' and r'-band photometry where possible, although when a single band is available we simply show $M_{g'}$ or $M_{r'}$ due to their similar central wavelength ($\lambda_V = 0.55$ μm, $\lambda_{g'} = 0.52$ μm, $\lambda_{r'} = 0.67$ μm).

The size-luminosity relation of the new dwarf candidates shows a similar slope as other nearby dwarfs on the literature, although they show a bias towards brighter μ_V, still sharing parameter space with other dwarf candidates on Centaurus A. However, the more compact and fainter dwarf is in a region almost without analogs.

Relatively high $\mu_V \sim 22$ mag arcsec^{-2} and $\sum_{eff,M_*} \sim 10^2$ $M_\odot pc^{-2}$ may indicate that, rather than being members of the Centaurus A group, these candidates may be members of a giant galaxy in the background. To check this possibility, we queried NED for any background source classified as a galaxy falling within 30′ of a dwarf candidate. This projected radius corresponds to a physical distance of ~ 200 kpc from a giant host located at a distance of 25 Mpc, so the diffuse nature of the dwarf galaxy can be easily spotted.

A potential background host for at least some of the dwarf galaxy candidates, is an interacting galaxy pair, NGC 5090 and NGC 5091, located near the center of the Centaurus A group at a distance of ~ 50 Mpc. Assuming this new distance, sizes and luminosities were recalculated and plotted as empty dashed stars in Figure 5.2, Figure 5.3, and Figure 5.4.

In Figure 5.2 the fainter dwarf candidates fall in the same region as the brighter dwarf galaxies in the Fornax cluster, while the brighter ones fall in a region without dwarf analogs. The same behavior is seen in the size-mass relation, Figure 5.3, most SCABS galaxy candidates are biased to higher densities lines compared to dwarfs from literature, and when comparing their properties at 50 Mpc, the brightest galaxies fall in locus almost devoid of analogs, along with some candidates more massive and more extended than UDGs, with values far from any known dwarf.

5.4 COLOR-MAGNITUDE RELATIONS

While color-magnitude diagrams (CMD) relation of stars is well related to stellar evolution theory, the optical spectra of galaxies are

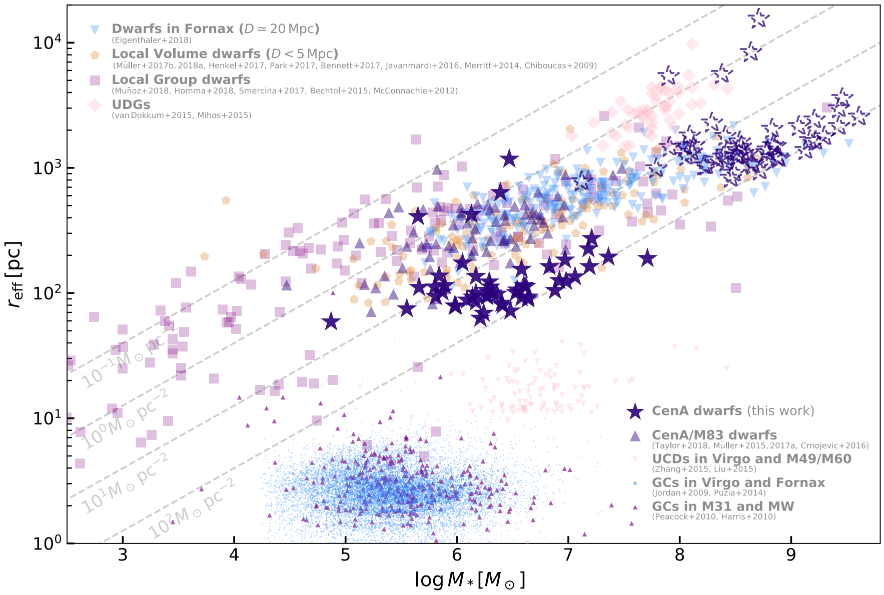

Figure 5.3: Size-Mass diagram displaying present dwarf galaxy candidates in Centaurus A, compared to other nearby dwarfs and other stellar systems (see legend). Dotted lines present iso-stellar mass surface density, $\sum_{eff,\mathcal{M}_*}$, ($M_\odot$ pc^{-2}). Empty dashed stars show this work galaxy sample shifted to a distance of 50 Mpc.

dominated by the integrated light from various generations of stellar populations. A copious amount of previous research has shown that there is a correlation of galaxy luminosity with star formation history (SFH), stellar initial mass function (IMF), chemical evolution, and/or dust attenuation. The CM relation is associated with a mass-metallicity relation since a more massive galaxy has a deeper potential well, and metals produced throughout their star-formation history are more easily retained (e.g. Ma et al. [34]).

Left panels of Figure 5.4 show $(u' - i')_0$, $(u' - g')_0$, and $(g' - i')_0$ vs. $M_{g'}$ CMDs of our dwarf galaxy sample, and compare them with dwarf galaxies in the Fornax cluster (Muñoz et al. [41]; Eigenthaler et al. [18]). We also plot nuclear star clusters (NSCs) corresponding to nucleated dwarf galaxies in the Fornax sample (Ordenes-Briceño et al. [49]), and compact stellar systems (CSSs) including ultra-compact dwarf galaxies (UCDs) and globular clusters (GCs) also confirmed in the Fornax cluster (Wittmann et al. [64]). A large sample of GCs from NGC 5128 (Taylor et al. [59]) are shown.

Dashed lines show the iso-$\mathcal{M}_*$ based on Bell et al. [3] color-$\mathcal{M}/L$ prescription for the different color combinations, using g' luminosities. Most dwarfs are concentrated on stellar masses $\sim 10^6$ M$_\odot$, reaching down to $\sim 10^5$ M$_\odot$, with lower values presented in $(u' - g')$ colors.

In all three plots our measurements lay on the faint end of Fornax dwarfs red sequence, presenting similar average colors in $(g' - i')_0$ CMD, while for $(u' - i')_0$ and $(u' - g')_0$ CMDs we present redder colors. The new NGC 5128 dwarf candidates present an offset of $\delta(u' - i')_0 \approx 0.3$ mag and $\delta(u' - g')_0 \approx 0.4$ mag. It appears our galaxy sample is more consistent with properties of NSCs and CSSs systems, despite their more extended and diffuse morphologies. Our targets might also be related to faint fuzzies, which are metal-rich apparently-old star clusters with unusually large radius (Chies-Santos, A. L. et al. [13]).

Luminosities calculated at a putative distance of 50 Mpc are similar to the brightest dwarfs in the Fornax galaxy cluster, presenting great color spread compared to Fornax dwarf's red sequence, especially in $(g' - i')$ CMD, where much redder colors are encountered without dwarf analogs. If we consider a significant number of these candidates to belong to background host like NGC 5090 or NGC 5091, which are significantly less massive than Fornax cluster, it would imply a very shallow slope for its faint-end galaxy luminosity function.

It is not possible to exclude these background galaxies to host many of these dwarf candidates, even though they would be hosting a population of bright galaxies only found so-far in galaxy cluster environments, suggesting most of them are indeed members of the Centaurus A group. Spectroscopic observations are needed to check group membership for all dwarf candidates.

5.5 STELLAR POPULATION PROPERTIES

Color-Magnitude diagrams (CMDs) are used to infer the mass assembly and star formation histories of galaxies (e.g., Zhang et al. [65]), and it is possible to constrain luminosity-weighted ages, metallicities, and stellar masses using multi-passband CMDs for large galaxy samples.

Scatter around the red sequence in CMD is related to different stellar populations in the sample, i.e., spread in ages and metallicities, and from photometric uncertainties. On right panels of Figure 5.4 we show histograms with its corresponding Epanechnikov-KDEs for our galaxy sample, along with other stellar systems (see legend). Symmetric distributions are observed around the peaks, with average colors $\langle(u' - i')\rangle = 2.05$, $\langle(u' - g')\rangle = 1.29$, and $\langle(g' - i')\rangle = 0.7$, with standard deviations of 0.41, 0.27, and 0.27, respectively. $(u' - i')$ present the greater scatter, suggesting color gradients on the sample.

When comparing color averages with other stellar systems in the plot, we note our Cen A candidates present similar values to compact

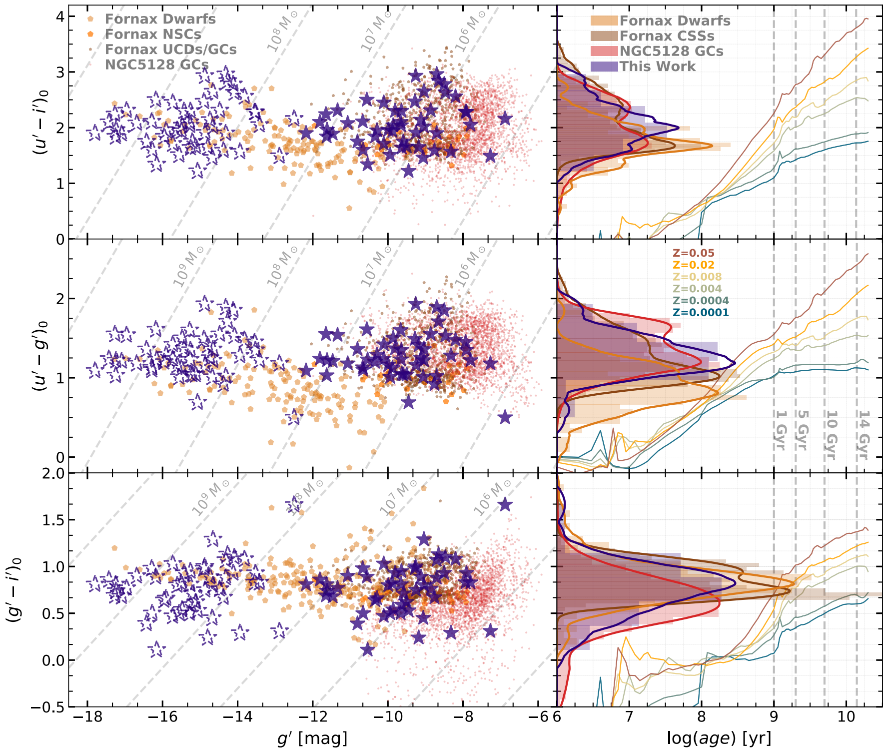

Figure 5.4: Color-magnitude diagrams and simple stellar populations model predictions for stellar populations of the SCABS galaxy sample. Left panels: $(u' - i')_0$, $(u' - g')_0$, and $(g' - i')_0$ vs. g CMDs. Dark stars show values for SCABS sample, compared to other stellar objects (see legend). Dashed lines show iso-$\mathcal{M}_*$ estimated from Bell et al. [3]. Right panels: Color distribution of SCABS galaxy sample, compared to other stellar systems. Overplotted SSP model prediction from Bruzual and Charlot [10] for metallicities in range $0.0001 < Z < 0.02$, along with vertical lines for ages 1, 5, 10, and 14 Gyr.

stellar systems (CCSs).

Ages of the galaxy sample are constrained by comparing broadband colors with predictions of simple stellar population (SSP) models of Bruzual and Charlot [10]. SSP model predictions for metallicities in the range $0.0001 < Z < 0.05$ as a function of age are displayed next to the sample color distribution.

The mass-metallicity relation from Kirby et al. [28] can be used to estimate metallicity of the galaxy sample,

$$\langle [Fe/H] \rangle = -1.69 + 0.30 \log(\mathcal{M}_*/10^6 M_\odot) \tag{5.4}$$

which is roughly continuous from the least massive system at $\mathcal{M}_* = 10^{3.5} M_\odot$ to the most massive giant ellipticals at $\mathcal{M}_* = 10^{12} M_\odot$.

Our most massive galaxy with $10^{7.71} M_{\odot}$ corresponds to a metallicity of $[Fe/H] \simeq -1.18$, and a $Z \simeq 0.001$.

For low metallicities $Z < 0.004$ we can expect ages of at least 10 Gyr for the average dwarf of our sample, as shown in the right pannel of $(g' - i')_0$ CMD in Figure 5.4. If we assume a uniformly old galaxy sample, a large spread in metallicities is expected, as shown in the plot. This phenomenon could be explained by different star formation histories along with the galaxy group, produced by their environment, or galaxy mergers. It is also important to take into account the age-metallicity degeneracy. Future spectroscopic observations would help constraining stellar population properties of the low mass galaxy sample.

Part III

SUMMARY AND FUTURE WORK

6 SUMMARY AND FUTURE WORK

We report the discovery of 51 new dwarf galaxy candidates based on the optical u′g′r′i′z′ imaging of 22 deg^2 centered on the nearby giant elliptical galaxy NGC 5128 as part of The Survey of Centaurus A's Baryonic Structures (SCABS), using the Dark Energy Camara (DECam) mounted on the 4-meter Blanco telescope at the Cerro Tololo Inter-American Observatory (CTIO) in Chile.

Dwarf galaxy candidates were identified by visual inspection of deep RGB image stacks performed by several people, and only candidates detected three or more times were considered for the study.

To summarize the main results:

- Morphological analysis of the dwarf galaxy population shows that surface brightness profiles are well represented with a single component Sérsic model with an average Sérsic index of $\langle n \rangle = 0.85 \pm 0.05$.
- Structural parameters show average sizes of $\langle r_e \rangle = 0.18 \pm 0.02$ kpc and round shapes with $\langle \epsilon \rangle \sim 0.25$. We note a preference towards vertical alignments, where only 17% of the candidates show $60 < PA < 120$.
- Stellar masses were calculated using color-derived mass-to-light ratios, obtaining an average stellar mass of log $\langle \mathcal{M}_* \rangle = 6.38 \pm 0.07$, spanning the range $4.8 \lesssim \log \mathcal{M}_*/M_\odot \lesssim 7.7$
- Scaling relations, r_e vs. M_V and log $\mathcal{M}_*$ show that our dwarf galaxy sample present similar slope to other dwarf galaxies in the literature. Although presenting relatively high $\mu_V \sim 22$ mag arcsec^{-2} and $\sum_{eff,\mathcal{M}_*} \sim 10^2$ $M_\odot pc^{-2}$. To guard against the possibility of being members of a background host, values were re-calculated considering a distance of 50 Mpc away. New values show similar luminosities to the brighter dwarfs in the Fornax cluster, while others seem more extended than UDGs, without dwarf analogs.
- If a great number of dwarf galaxy candidates actually belong to background galaxies NGC 5090 or NGC 5091, which are significantly less massive than Fornax cluster, it will imply a very shallow slope for its faint-end galaxy luminosity function.

- The identified galaxy sample is more consistent with properties of NSCs and CSSs systems, rather than Fornax cluster dwarfs, despite their more extended and diffuse morphologies.
- The most massive galaxy of the sample has $10^{7.7}$ $M_{\odot}$, corresponding to a metallicity $[Fe/H] \simeq -1.18$, and to $Z \simeq 0.001$.
- Bruzual and Charlot SSP models for low metallicities ($Z < 0.004$) in $(g' - i')$ CMDs predict average ages of at least 10 Gyr. Assuming old ages, a large spread in metallicities is expected, probably due to different star formation histories.

For future work, an inspection of the outer ring from observations made in the Survey of Centaurus A's Baryonic Structures (SCABS), with the corresponding characterization of dwarf candidates discovered on these tiles. This will lead to a complete census of the dwarf galaxy population from the entire Centaurus A Galaxy Group.

Spectroscopic observations are needed to check group membership for all dwarf candidates, and to break the age-metallicity degeneracy.

Confirmed membership would result in an interesting sample of dwarf galaxies with high μ_e and $\sum_{eff,\mathcal{M}_*}$ with similar properties to CSSs for deeper in-depth follow-up studies.

Part IV

APPENDIX

A

DWARF MODELING

Dwarf galaxy surface-brightness modeling with *GALFIT*. Each set of images shows the modeling process for each dwarf in Centaurus A, presenting the dwarf galaxy (top pannels), the corresponding 2D Sérsic model (middle pannels), and the residual image, i.e. galaxy-model (lower pannels) for every passband ($u'g'r'i'z'$ from left to right). Only the spheroid component is modeled for nucleated dwarfs so that the nuclear star cluster is visible in the residual images.

Section A.1 shows 51 new dwarf galaxy candidates presented in this work, while Section A.2 shows all confirmed and known dwarf galaxies in Centaurus A, including those dwarfs unable to fit with the *GALFIT* software.

A.1 NEW DWARF CANDIDATES IN CEN A

Dwarf galaxy surface-brightness modeling of the 51 new dwarf galaxies presented in this work.

SCABS131200-422827

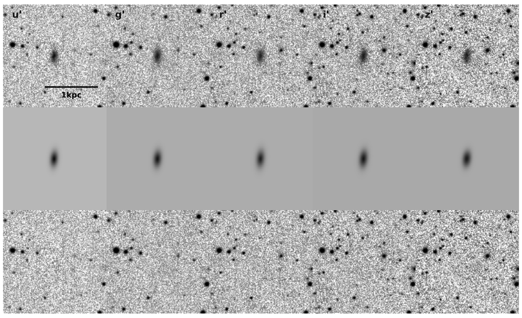

SCABS131230-420328

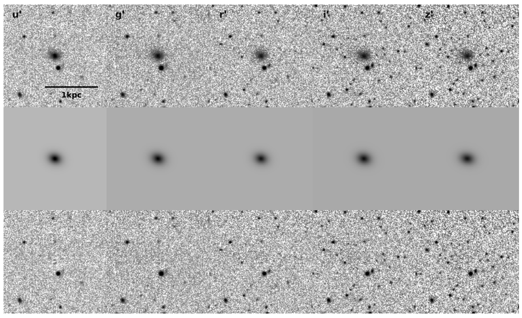

SCABS131350-422432

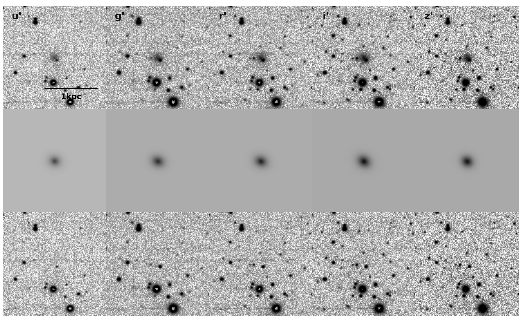

SCABS131359-415806

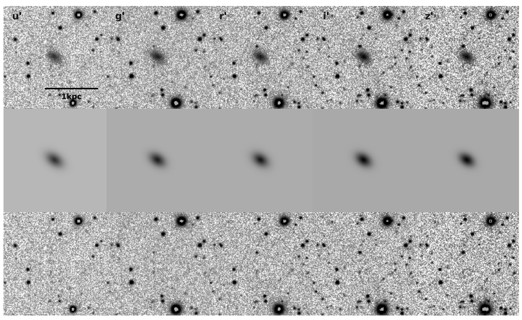

SCABS131545-434350

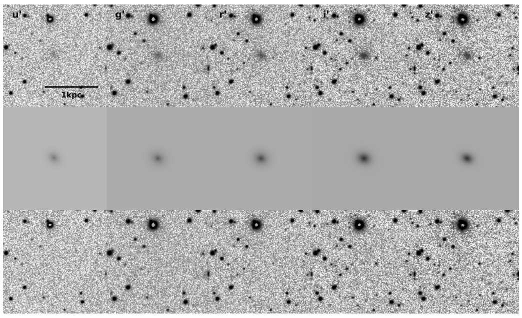

SCABS131727-432210

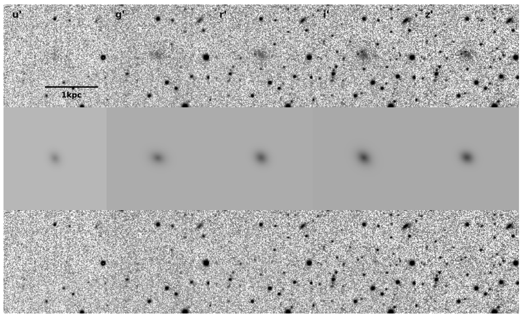

SCABS131815-430639

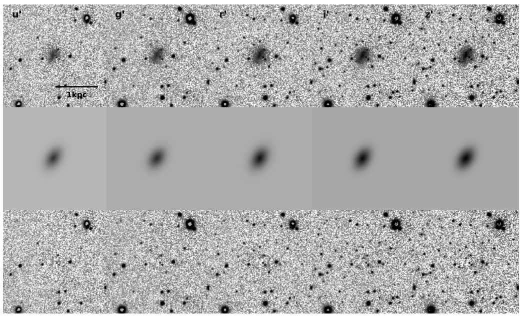

SCABS131902-434417

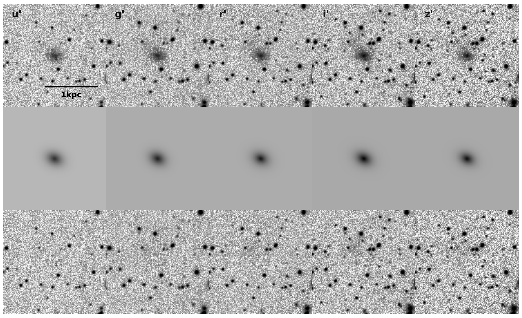

SCABS131902-430749

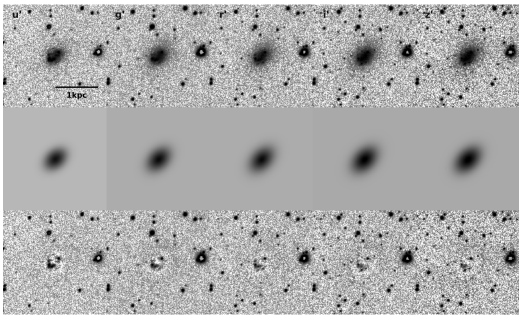

SCABS131905-432305

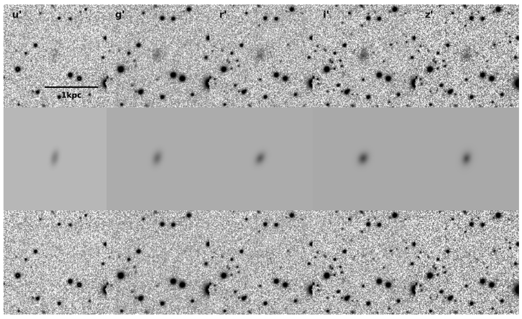

SCABS132037-433556

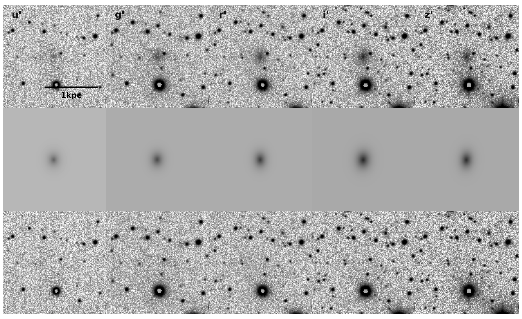

SCABS132049-423553

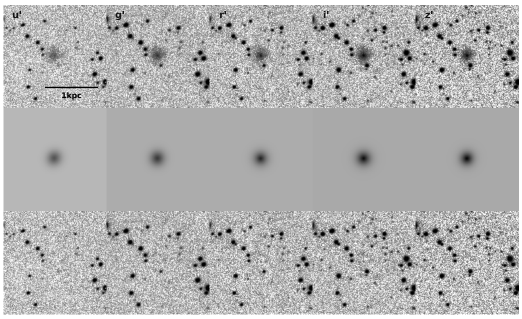

SCABS132109-433619

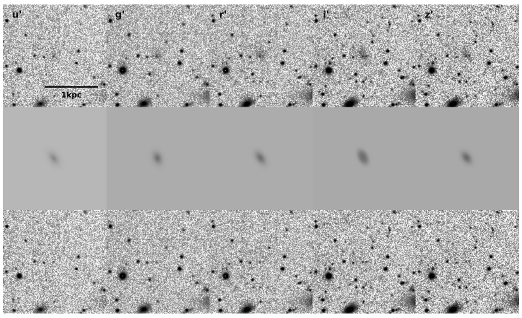

SCABS132138-435424

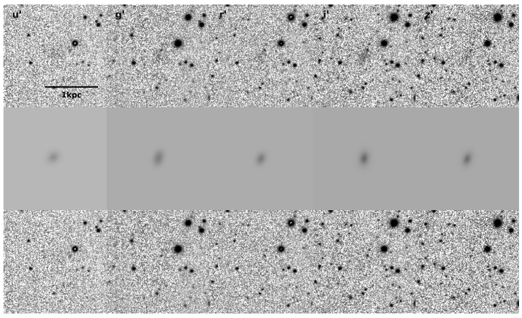

SCABS132156-401938

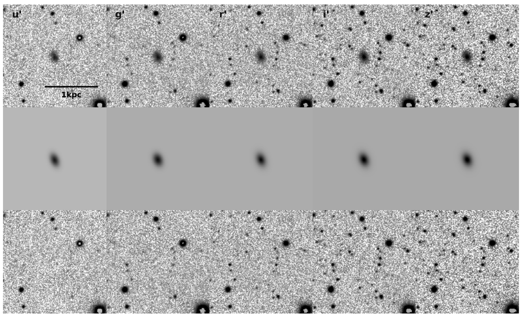

SCABS132207-403141

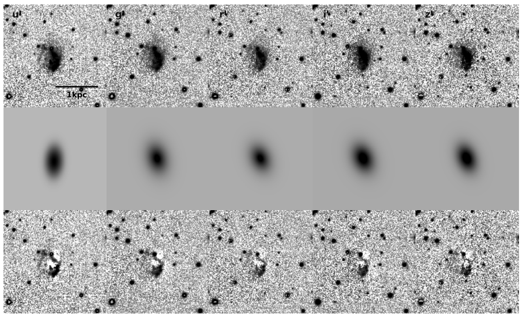

SCABS132210-433256

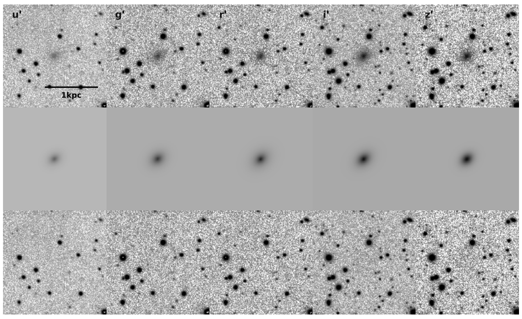

SCABS132213-401734

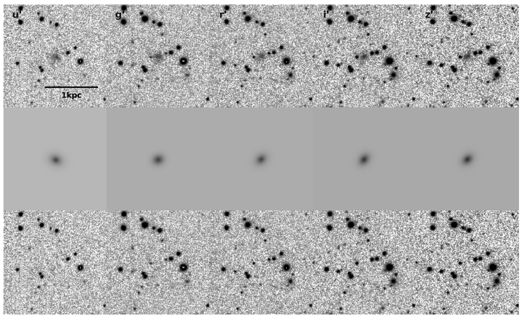

SCABS132237-403437

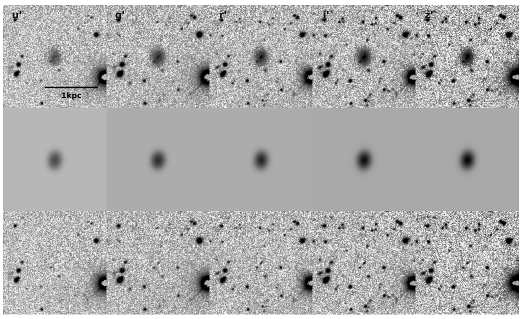

SCABS132245-413224

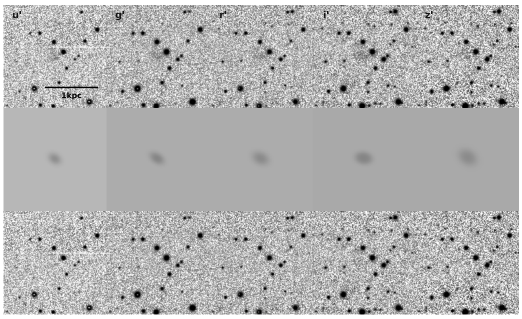

SCABS132311-430153

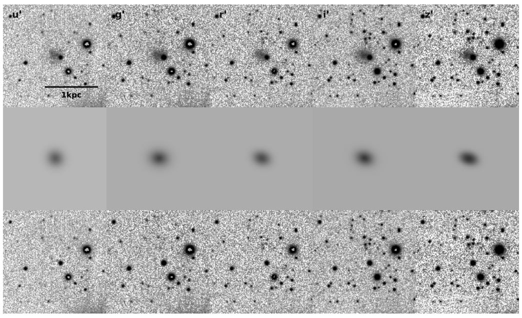

SCABS132345-433920

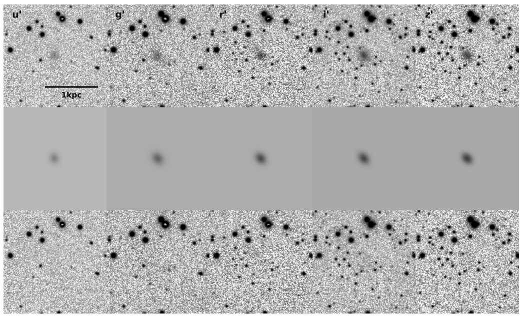

SCABS132431-432816

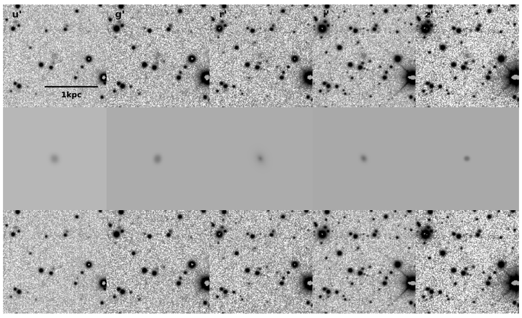

SCABS132456-434012

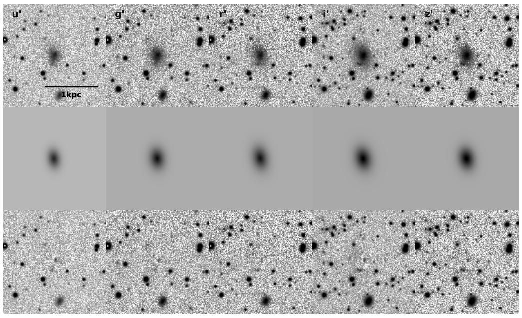

SCABS132456-422247

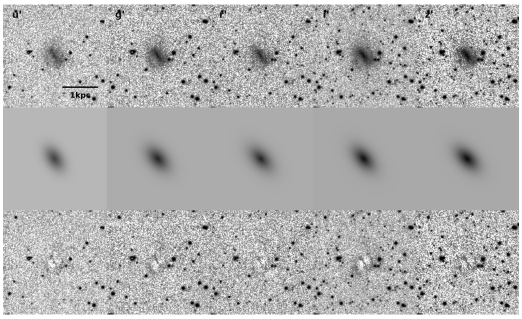

SCABS132517-421829

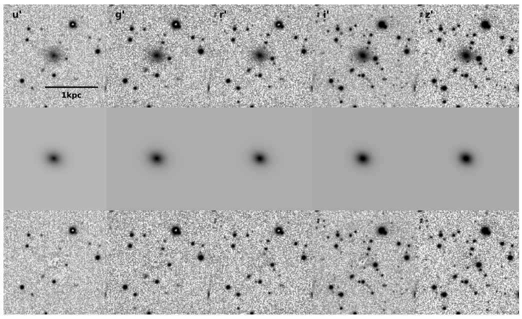

SCABS132540-404150

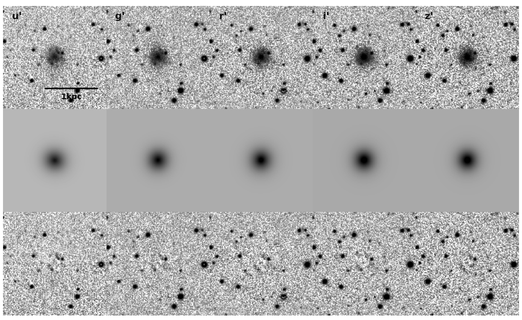

SCABS132611-441557

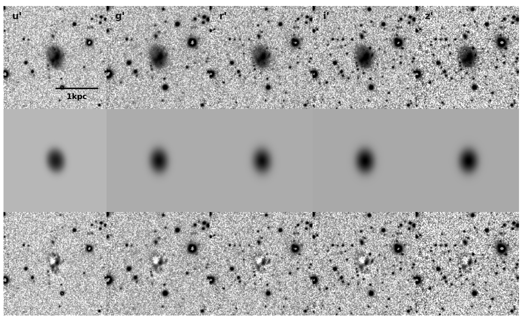

SCABS132631-405530

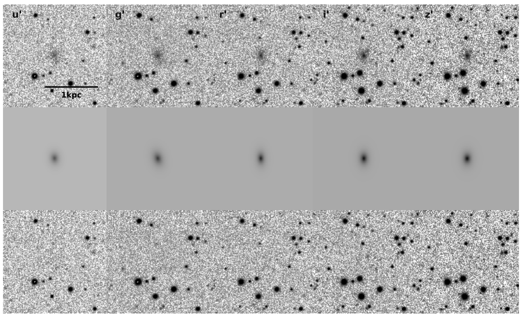

SCABS132704-431951

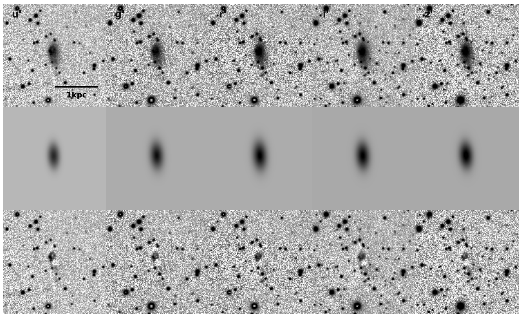

SCABS132711-423024

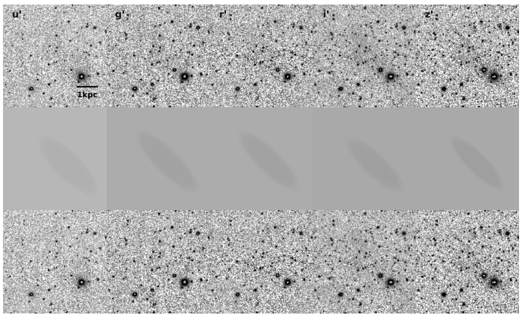

SCABS132725-404911

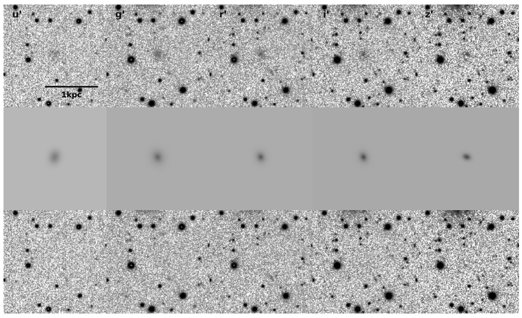

SCABS132745-420614

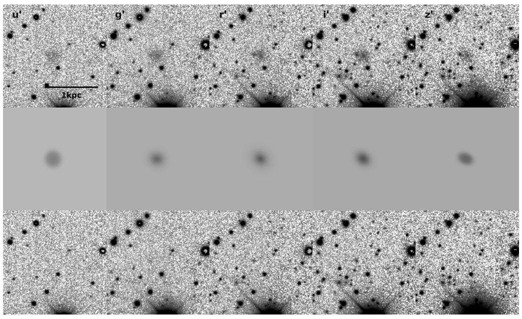

SCABS132804-420834

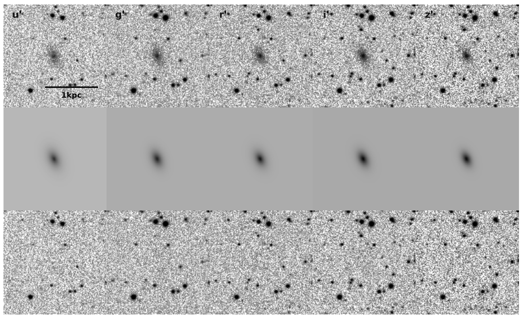

SCABS132835-415414

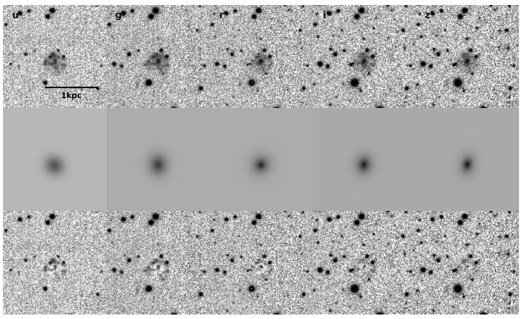

SCABS132850-420504

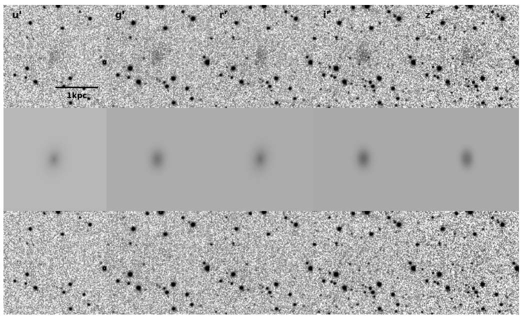

SCABS132916-450607

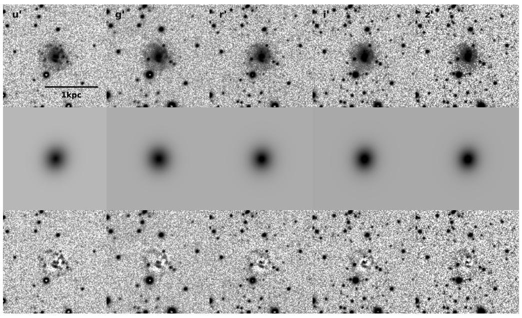

SCABS132927-435740

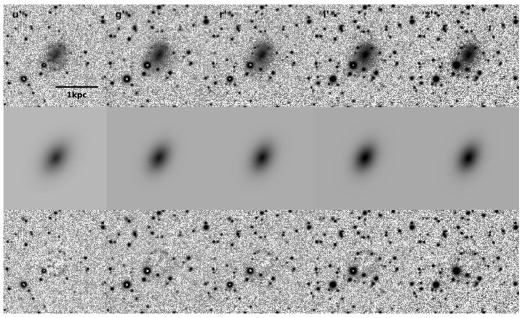

SCABS133032-442318

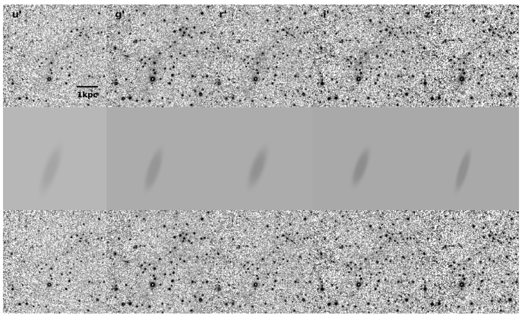

SCABS133035-442641

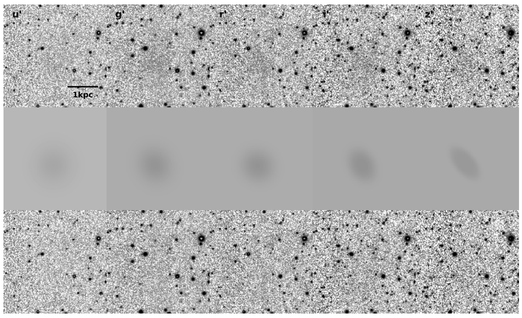

SCABS133042-444101

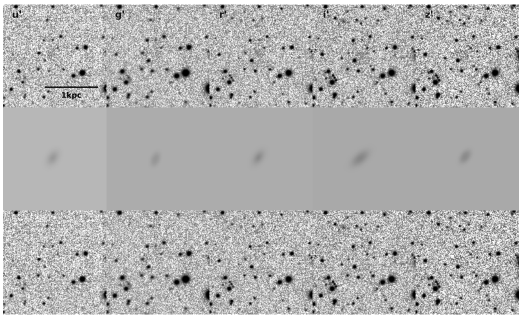

SCABS133120-423211

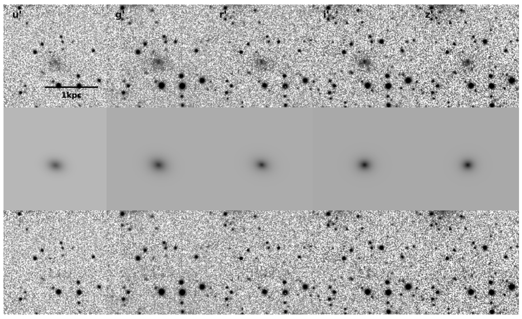

SCABS133141-435026

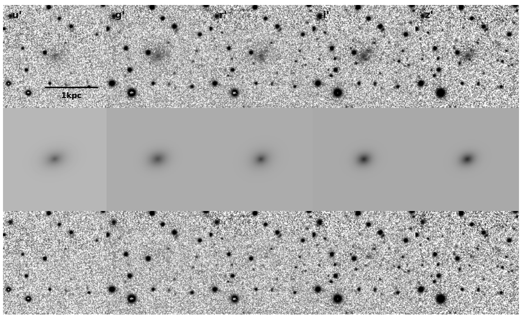

SCABS133145-423038

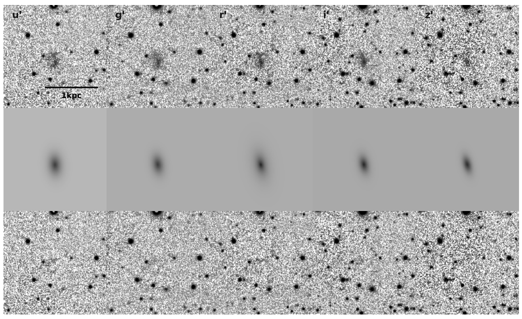

SCABS133151-441824

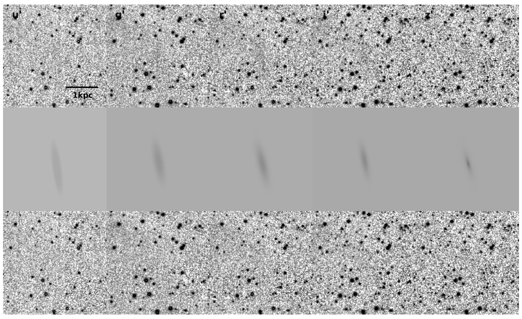

SCABS133214-431727

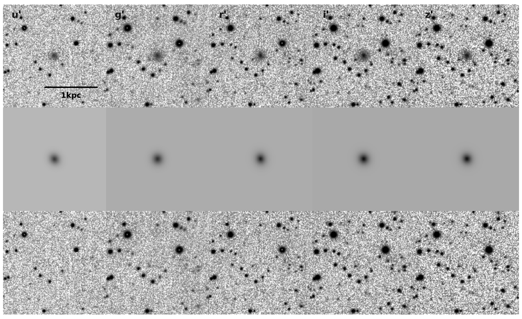

SCABS133301-410903

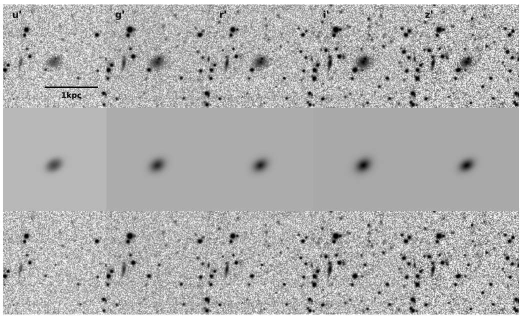

SCABS133307-425205

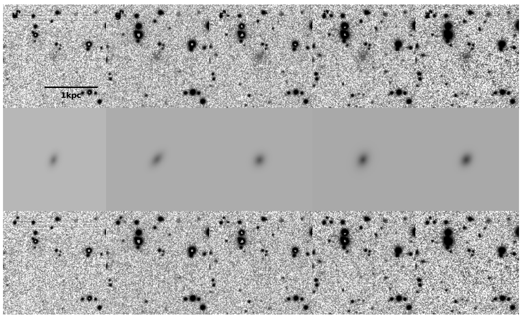

SCABS133503-415507

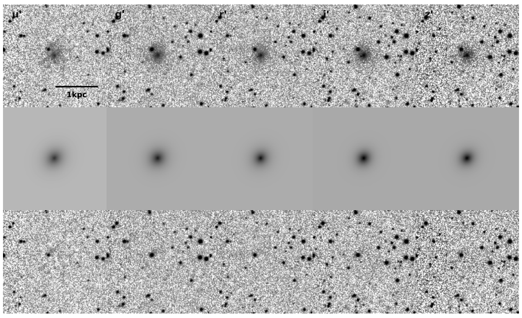

SCABS133523-412043

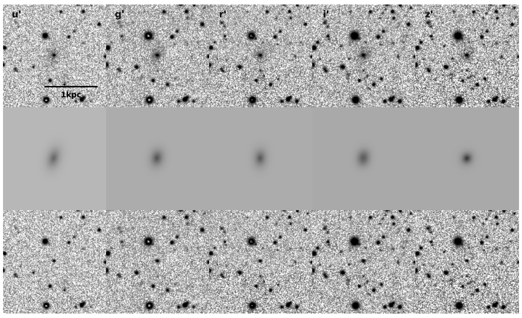

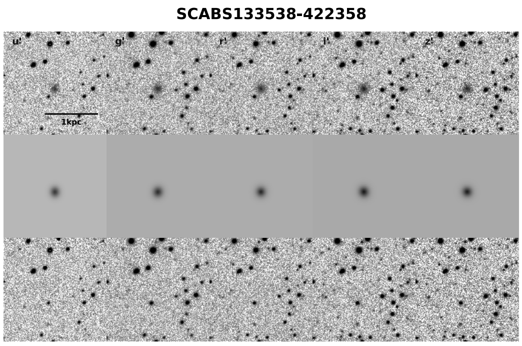

Figure A.1: New dwarf candidates' surface-brightness modeling with *GALFIT*. Each set of figures correspond to a single dwarf galaxy candidate modeling. The process shows the dwarf galaxy (top pannels), the corresponding 2D Sérsic model (middle pannels), and the residual image, i.e. galaxy-model (lower pannels). Dwarf-model-residual images are shown in u', g', r', i', and z' frames (left to right). Only the spheroid component of SCABS133523-412043 is modeled, its nuclear star cluster is visible in the residual image.

A.2 CONFIRMED DWARFS AND KNOWN CANDIDATES

Dwarf galaxy surface-brightness modeling of confirmed and known candidates in Centaurus A, presented in Karachentsev, Makarov, and Kaisina [25], Crnojević et al. [15], Crnojević et al. [16], Crnojević et al. [17], Müller, Jerjen, and Binggeli [44], and Taylor et al. [60].

T18-dw1312-4247

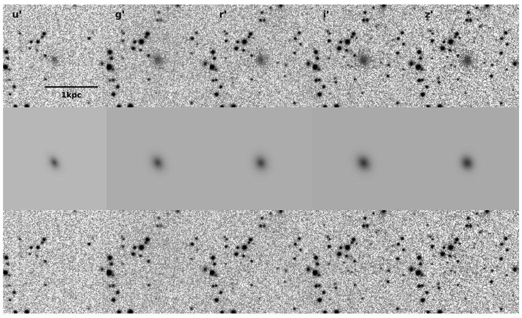

T18-dw1312-4247

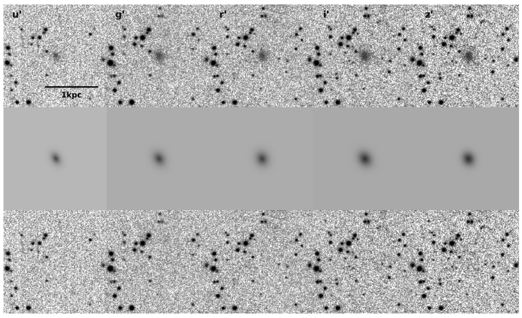

T18-dw1312-4219

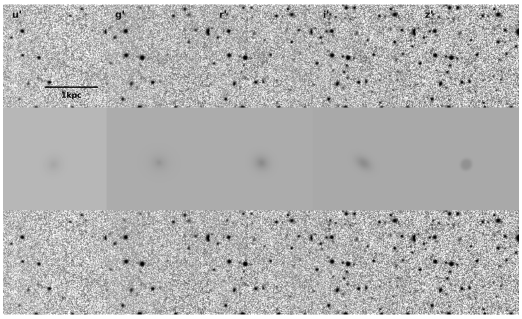

T18-dw1313-4247

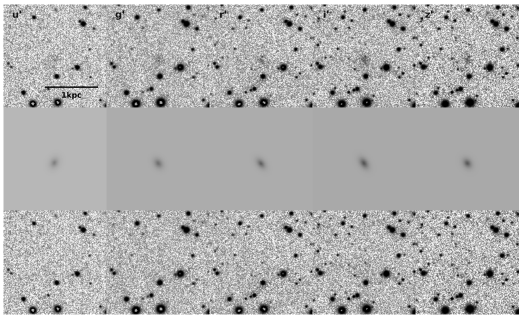

KK189

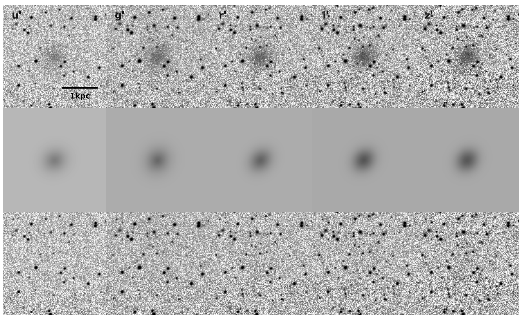

T18-dw1314-4211

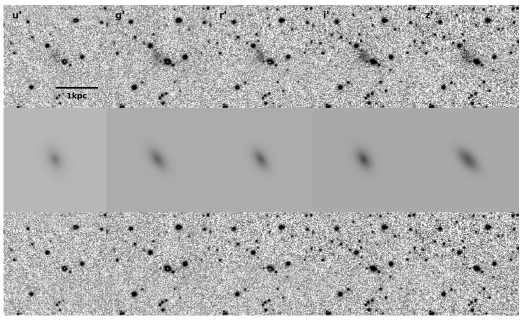

T18-dw1314-4214

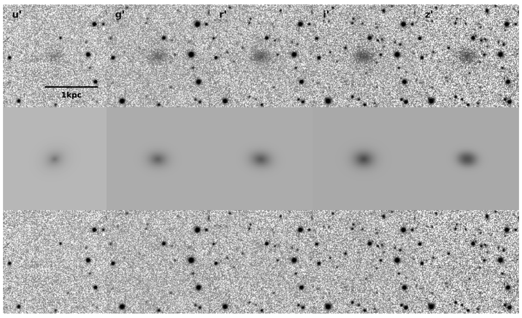

T18-dw1314-4204

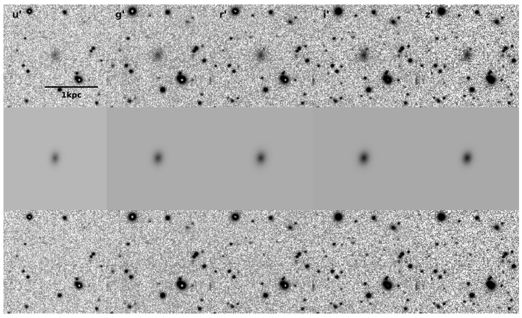

T18-dw1314-4230

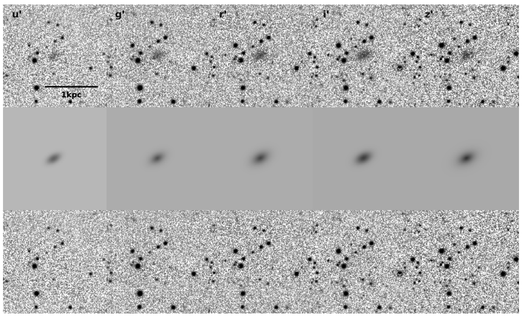

T18-dw1315-4142

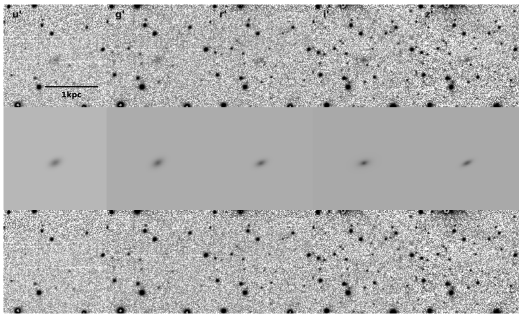

T18-dw1315-4232

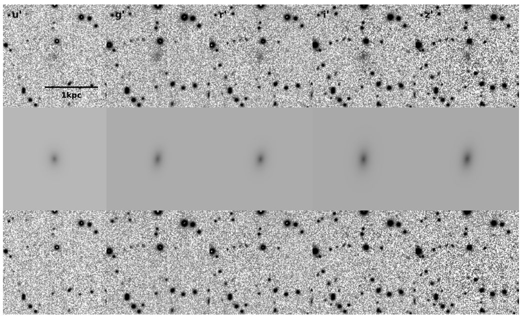

T18-dw1316-4309

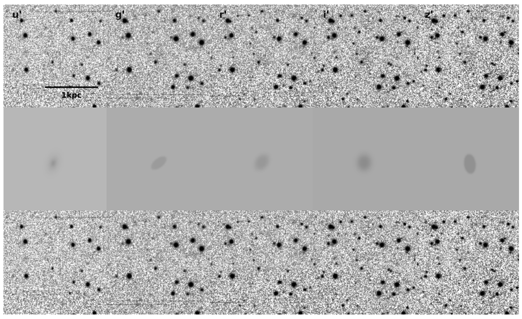

T18-dw1317-4224

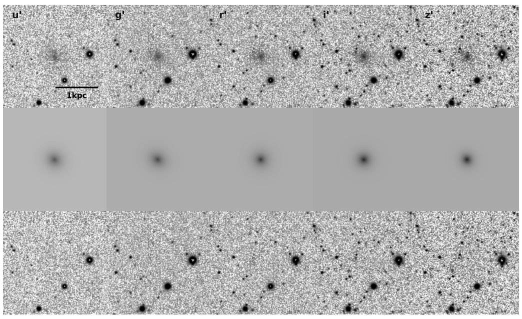

T18-dw1318-4256

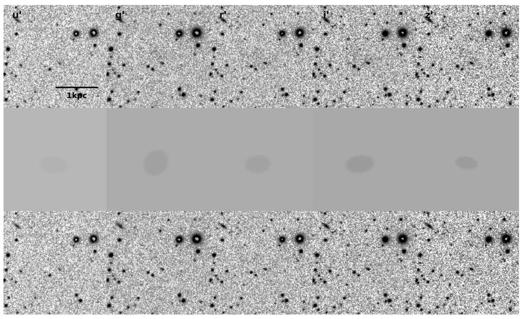

T18-dw1318-4234

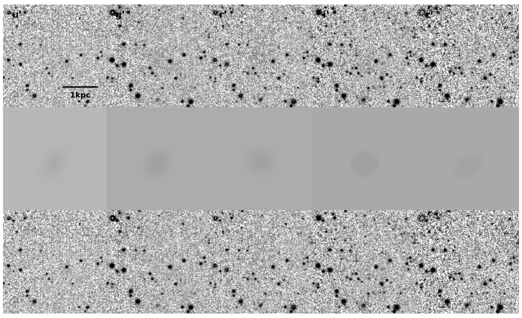

dw1318-44

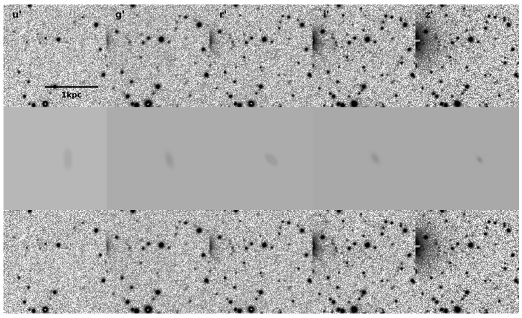

T18-dw1319-4203

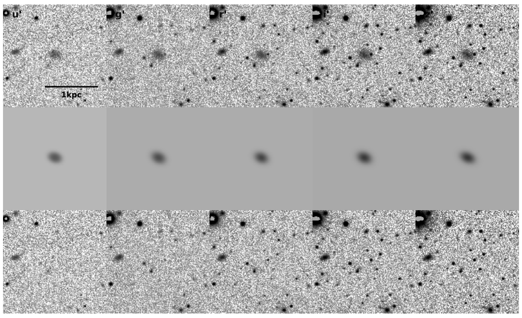

KK197

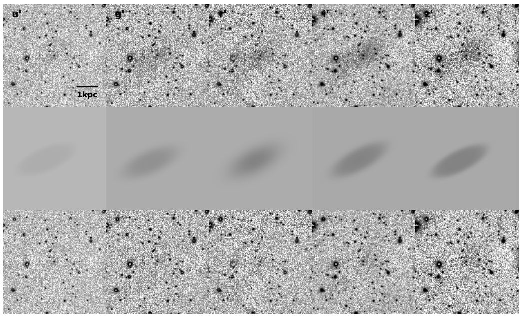

[KK2000]55

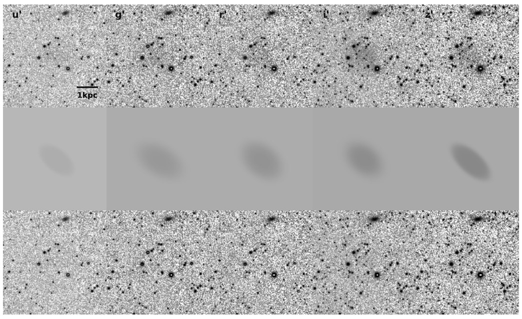

CenA-MM-Dw4

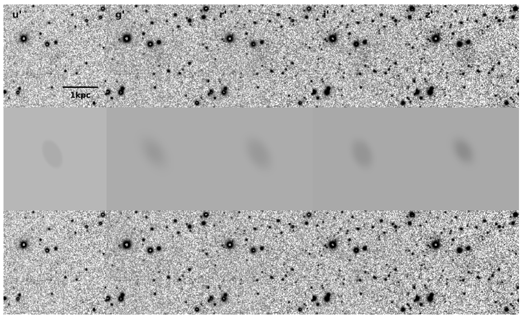

dw1323-40b

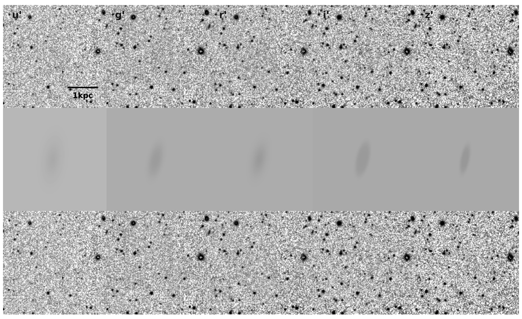

dw1323-40

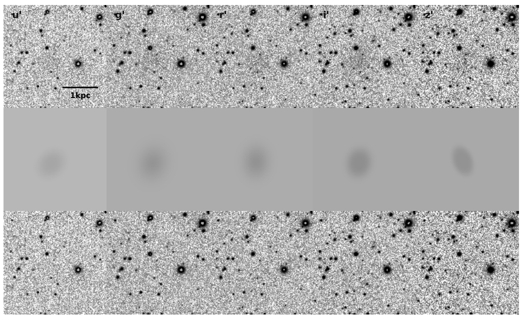

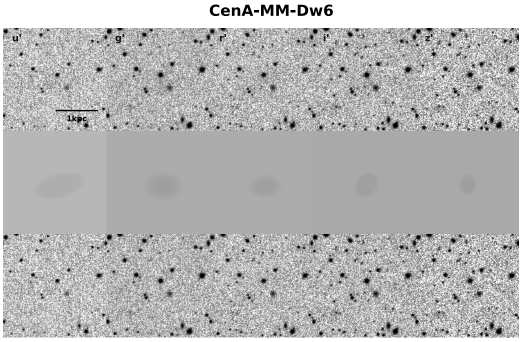
CenA-MM-Dw6
1kpc

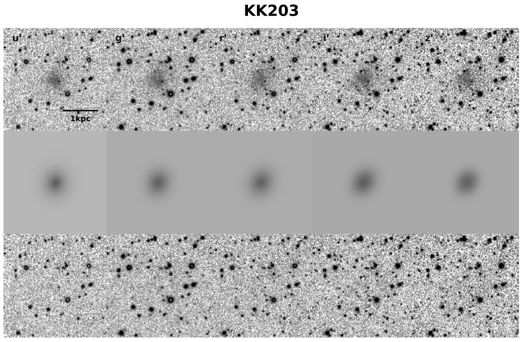
KK203
1kpc

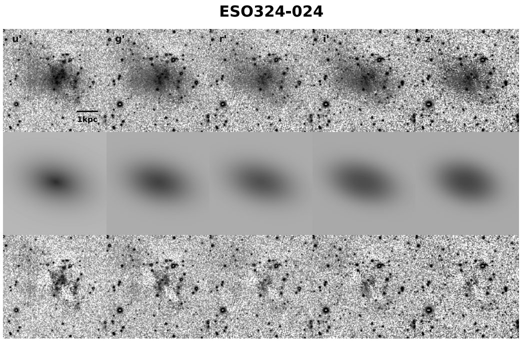
ESO324-024
1kpc

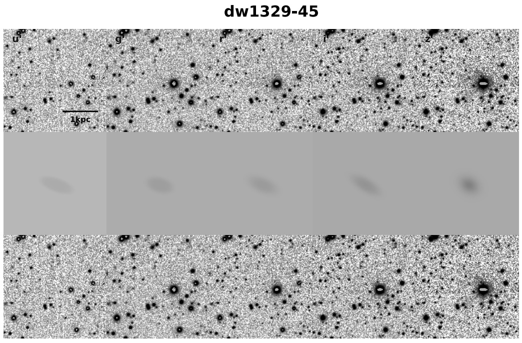
dw1329-45
1kpc

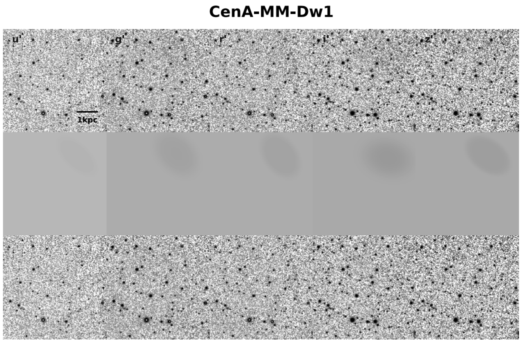
CenA-MM-Dw1
1kpc

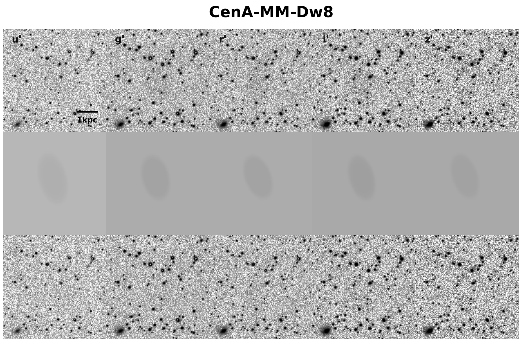
CenA-MM-Dw8
1kpc

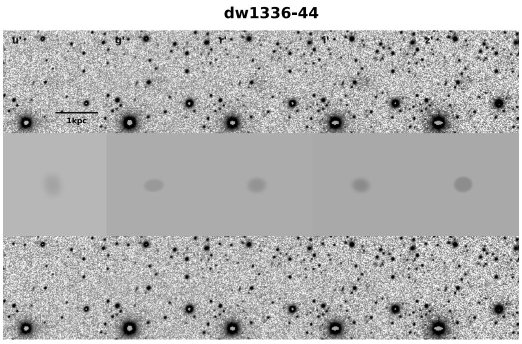
dw1336-44
1kpc

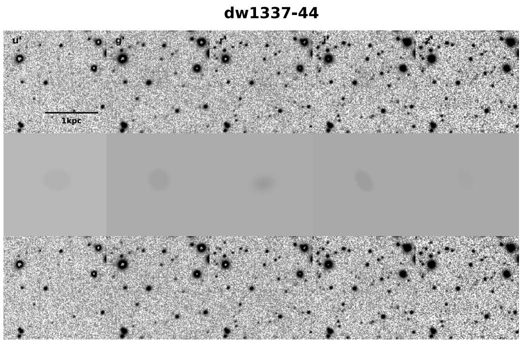
dw1337-44
1kpc

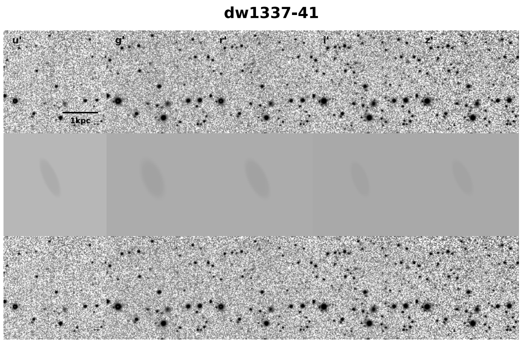

Figure A.2: Confirmed and known dwarf candidates' surface-brightness modeling with *GALFIT*. Each set of figures correspond to a single dwarf galaxy candidate modeling. The process shows the dwarf galaxy (top pannels), the corresponding 2D Sérsic model (middle pannels), and the residual image, i.e. galaxy-model (lower pannels). Dwarf-model-residual images are shown in u', g', r', i', and z' frames (left to right).

A.2.1 *Fainter Dwarfs in the Sample*

Due to their faint nature, *GALFIT* was unable to fit CenA-MM-Dw2, CenA-MM-Dw3, CenA-MM-Dw5, CenA-MM-Dw7, CenA-MM-Dw9, CenA-MM-Dw10, and dw1323-40c, listed in Table 3.2 and Table 3.3. The following figures show these dwarf galaxies in the u', g', r', i', and z' frames (from left to right). Given the depth of our observations we are unable to detect these dwarf galaxies.

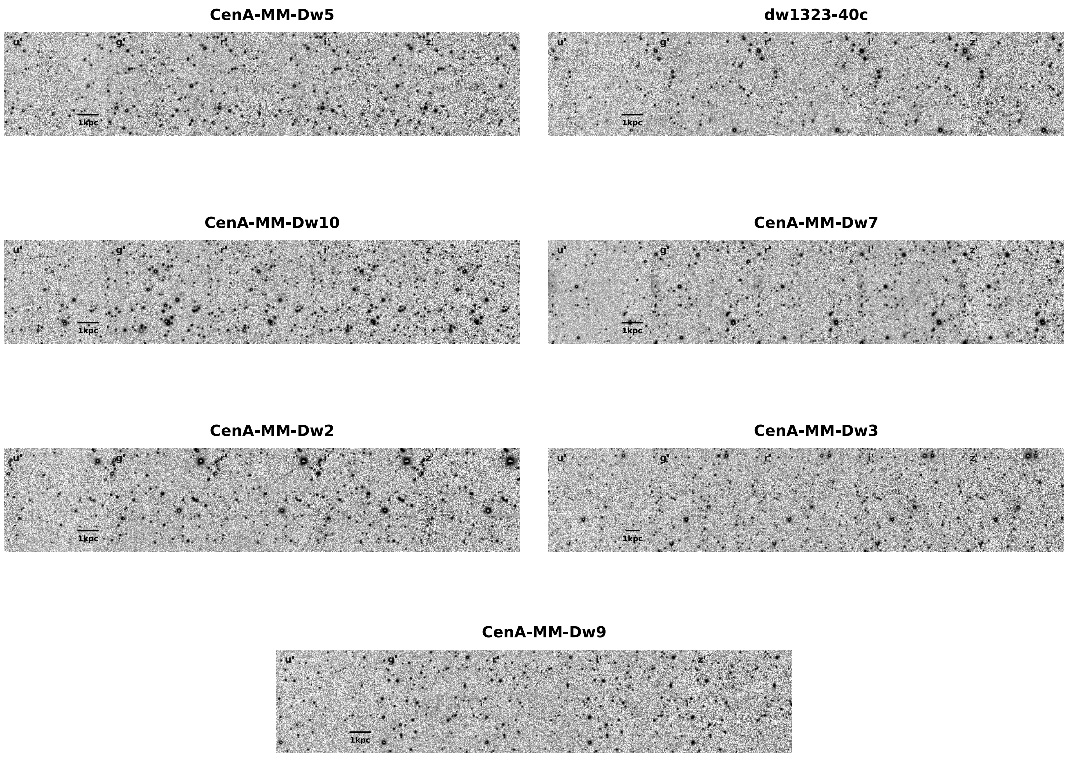

Figure A.3: Confirmed and known dwarf candidates' surface-brightness not modeled with *GALFIT*. Each set of figures correspond to a single dwarf galaxy in u', g', r', i', and z' frames (left to right). Given the depth of our observations we are unable to detect these dwarf galaxies.

B

STRUCTURAL PARAMETERS OF THE DWARF GALAXY SAMPLE

Photometric and structural parameters are listed in Table B.1 and Table B.2, distinguishing if it is a new or known dwarf.

Photometric results are listed in Table B.1, including galaxy coordinates, all available galaxy surface brightness (μ, mag arcsec^2) derived with *GALFIT*, absolute V-band magnitudes, and estimated total stellar masses ($\mathcal{M}_*$, in $M_\odot$).

Structural parameters in all available filters are listed in Table B.2, we present effective radius (r_e, in kpc), Sérsic index (n), ellipticity (ϵ), and position angle (PA), along with the total effective radius of the galaxy.

Table B.1: Photometric Parameters and Mass of Centaurus A's Dwarf Galaxies

ID	REFERENCE	α	δ	μ_u	μ_g	μ_r	μ_i	μ_z	M_V	LOG $\mathcal{M}_*$
SCABS131200-422827	——	$13^h12^m00^s.22$	-42°28′27″.15	25.26	24.36	24.72	23.86	23.78	-9.52	6.27
SCABS131210-424649	T18-dw1312-4247	$13^h12^m10^s.18$	-42°46′48″.53	26.24	25.05	24.99	24.01	23.87	-9.15	6.33
SCABS131210-424648	T18-dw1312-4247	$13^h12^m10^s.30$	-42°46′48″.30	26.24	25.05	24.98	24.01	23.88	-9.15	6.33
SCABS131222-421842	T18-dw1312-4219	$13^h12^m22^s.48$	-42°18′41″.58	28.63	27.69	26.70	26.26	25.47	-7.93	5.27
SCABS131230-420328	——	$13^h12^m29^s.58$	-42°03′28″.31	24.68	23.91	24.24	23.48	23.66	-9.76	6.40
SCABS131243-424651	T18-dw1313-4247	$13^h12^m42^s.87$	-42°46′50″.57	27.48	25.93	25.96	24.97	24.95	-7.79	5.78
SCABS131245-414956	KK189	$13^h12^m45^s.24$	-41°49′55″.89	26.85	25.51	25.43	24.41	24.45	-10.69	6.88
SCABS131334-421110	T18-dw1314-4211	$13^h13^m34^s.27$	-42°11′10″.09	27.58	26.02	25.90	24.98	25.11	-9.65	6.76
SCABS131336-421408	T18-dw1314-4214	$13^h13^m36^s.41$	-42°14′08″.33	27.47	25.67	25.55	24.60	24.42	-9.39	6.42
SCABS131350-422432	——	$13^h13^m49^s.65$	-42°24′32″.28	26.06	24.57	24.49	23.52	23.42	-9.31	6.41
SCABS131359-415806	——	$13^h13^m58^s.93$	-41°58′05″.73	25.62	24.18	24.25	23.23	23.24	-9.98	6.53
SCABS131408-420410	T18-dw1314-4204	$13^h14^m08^s.18$	-42°04′9.″90	26.35	24.77	24.77	23.73	23.67	-9.04	6.22
SCABS131422-423043	T18-dw1314-4230	$13^h14^m21^s.89$	-42°30′43″.28	26.44	25.45	25.37	24.30	24.63	-9.03	6.12
SCABS131445-414228	T18-dw1315-4142	$13^h14^m44^s.82$	-41°42′28″.27	26.94	25.72	25.84	25.30	25.20	-7.75	5.66
SCABS131503-423218	T18-dw1315-4232	$13^h15^m02^s.98$	-42°32′18″.28	27.54	26.21	26.32	25.57	25.39	-8.65	6.32
SCABS131534-430927	T18-dw1316-4309	$13^h15^m33^s.97$	-43°09′27″.18	28.41	26.90	26.71	25.54	25.82	-7.17	5.89
SCABS131545-434350	——	$13^h15^m45^s.29$	-43°43′50″.15	27.53	26.10	25.58	24.19	24.27	-8.79	6.17
SCABS131642-422406	T18-dw1317-4224	$13^h16^m42^s.27$	-42°24′05″.96	26.85	25.78	25.69	24.53	24.38	-9.88	6.27
SCABS131727-432210	——	$13^h17^m27^s.10$	-43°22′10″.20	27.21	25.78	25.32	24.51	24.35	-8.73	6.32
SCABS131748-425540	T18-dw1318-4256	$13^h17^m48^s.49$	-42°55′40″.45	29.08	26.81	27.32	26.41	26.58	-8.06	6.24
SCABS131806-423337	T18-dw1318-4234	$13^h18^m05^s.59$	-42°33′37″.10	29.38	27.36	27.51	26.55	27.53	-8.63	5.58
SCABS131815-430639	——	$13^h18^m15^s.47$	-43°06′39″.36	25.84	24.46	24.27	23.50	23.39	-10.85	6.83
SCABS131858-445341	dw1318-44	$13^h18^m58^s.00$	-44°53′41″.00	28.73	27.31	27.19	26.37	26.25	-6.53	4.68
SCABS131902-434417	——	$13^h19^m01^s.94$	-43°44′16″.56	25.76	24.49	24.71	23.70	23.87	-9.84	6.54
SCABS131902-430749	——	$13^h19^m02^s.08$	-43°07′49″.22	24.68	23.66	23.86	22.96	22.95	-11.80	7.36

CONTINUED ON NEXT PAGE

Table B.1 – continued from previous page

ID	REFERENCE	α	δ	μ_u	μ_g	μ_r	μ_i	μ_z	M_V	LOG $\mathcal{M}_*$
SCABS131905-432305	——	$13^h19^m05^s.01$	-43°23′05″.10	27.23	25.68	25.44	24.23	24.64	-8.24	6.09
SCABS131921-420339	T18-dw1319-4203	$13^h19^m21^s.30$	-42°03′39″.50	25.63	24.62	24.62	23.79	23.88	-9.09	6.29
SCABS131952-415937	CenA-MM-Dw5	$13^h19^m52^s.40$	-41°59′37″.00	—	—	—	—	—	—	—
SCABS132037-433556	——	$13^h20^m36^s.94$	-43°35′55″.92	27.06	25.34	25.26	24.25	24.49	-9.13	6.62
SCABS132049-423553	——	$13^h20^m49^s.30$	-42°35′52″.80	25.86	24.41	24.41	23.41	23.33	-9.64	6.58
SCABS132109-433619	——	$13^h21^m09^s.30$	-43°36′18″.88	27.79	25.82	26.01	24.92	25.11	-7.92	5.81
SCABS132138-435424	——	$13^h21^m38^s.13$	-43°54′23″.80	27.45	26.10	26.06	25.21	25.44	-7.73	6.14
SCABS132140-430457	CenA-MM-Dw11b	$13^h21^m40^s.10$	-43°04′57″.00	—	—	—	—	—	—	—
SCABS132156-401938	——	$13^h21^m55^s.60$	-40°19′38″.10	25.03	23.72	23.98	22.99	22.99	-9.61	6.48
SCABS132202-423209	KK197	$13^h22^m01^s.88$	-42°32′09″.05	29.02	26.93	26.61	25.93	25.83	-11.89	7.26
SCABS132207-403141	——	$13^h22^m07^s.12$	-40°31′41″.35	24.52	23.64	23.73	22.55	22.54	-12.02	7.71
SCABS132210-433256	——	$13^h22^m10^s.38$	-43°32′55″.81	26.89	25.16	25.29	24.00	23.61	-9.37	6.36
SCABS132212-424359	[KK2000]55	$13^h22^m12^s.21$	-42°43′58″.60	28.61	26.85	26.49	25.69	25.70	-11.40	7.11
SCABS132213-401734	——	$13^h22^m12^s.80$	-40°17′34″.10	26.23	24.68	25.20	24.23	24.20	-8.69	5.98
SCABS132237-403437	——	$13^h22^m36^s.70$	-40°34′37″.30	25.51	23.94	23.99	22.97	22.89	-10.12	6.88
SCABS132245-413224	——	$13^h22^m45^s.30$	-41°32′24″.20	27.18	26.15	26.38	25.40	25.78	-7.84	5.66
SCABS132303-414710	CenA-MM-Dw4	$13^h23^m02^s.60$	-41°47′10″.00	28.38	27.30	27.15	26.17	26.00	-9.29	6.06
SCABS132311-430153	——	$13^h23^m10^s.83$	-43°01′53″.16	25.92	24.77	24.85	24.00	23.80	-9.61	6.60
SCABS132337-404317	dw1323-40c	$13^h23^m37^s.00$	-40°43′17″.00	—	—	—	—	—	—	—
SCABS132345-433920	——	$13^h23^m45^s.41$	-43°39′20″.11	26.83	25.24	24.76	24.18	23.94	-8.62	5.99
SCABS132355-405009	dw1323-40b	$13^h23^m55^s.00$	-40°50′09″.00	29.49	27.76	28.01	26.97	27.13	-9.05	5.71
SCABS132411-420827	CenA-MM-Dw12b	$13^h24^m10^s.71$	-42°08′27″.22	27.93	26.41	26.30	25.25	24.79	-8.62	6.17
SCABS132431-432816	——	$13^h24^m30^s.96$	-43°28′16″.28	26.86	25.47	26.72	24.84	24.36	-7.41	4.87
SCABS132433-444407	CenA-MM-Dw10	$13^h24^m32^s.90$	-44°44′07″.10	—	—	—	—	—	—	—
SCABS132453-404535	dw1323-40	$13^h24^m53^s.44$	-40°45′34″.63	27.97	26.78	26.76	25.57	25.94	-9.86	6.22

CONTINUED ON NEXT PAGE

Table B.1 – continued from previous page

ID	REFERENCE	α	δ	μ_u	μ_g	μ_r	μ_i	μ_z	M_V	LOG $\mathcal{M}_*$
SCABS132456-434012	——	$13^h24^m56^s.08$	-43°40′12″.12	25.47	24.12	24.44	23.35	23.25	-10.54	6.92
SCABS132456-422247	——	$13^h24^m56^s.45$	-42°22′46″.52	26.11	24.77	25.11	24.05	23.94	-11.58	7.21
SCABS132517-421829	——	$13^h25^m17^s.20$	-42°18′28″.54	25.56	23.97	23.98	23.02	22.82	-10.20	6.64
SCABS132540-404150	——	$13^h25^m39^s.69$	-40°41′49″.93	25.06	23.68	23.67	22.70	22.73	-11.14	6.98
SCABS132558-410539	CenA-MM-Dw6	$13^h25^m57^s.60$	-41°05′39″.00	28.77	26.96	27.23	26.62	26.48	-8.55	5.21
SCABS132611-441557	——	$13^h26^m11^s.39$	-44°15′57″.20	24.55	23.48	23.63	22.73	22.73	-11.57	7.19
SCABS132629-433324	CenA-MM-Dw7	$13^h26^m28^s.70$	-43°33′24″.00	—	—	—	—	—	—	—
SCABS132631-405530	——	$13^h26^m30^s.69$	-40°55′29″.51	26.66	25.44	25.41	24.30	24.25	-8.79	6.17
SCABS132649-430002	CenA-MM-Dw10b	$13^h26^m49^s.36$	-43°00′02″.04	28.80	26.86	26.32	25.83	25.86	-7.74	5.27
SCABS132704-431951	——	$13^h27^m03^s.92$	-43°19′51″.30	25.49	24.16	24.04	23.33	23.15	-11.46	6.97
SCABS132711-423024	——	$13^h27^m10^s.61$	-42°30′24″.33	29.50	28.30	28.22	27.61	27.65	-10.80	6.47
SCABS132725-404911	——	$13^h27^m25^s.21$	-40°49′10″.73	26.83	25.85	25.61	24.67	24.35	-8.10	5.55
SCABS132728-452111	KK203	$13^h27^m27^s.86$	-45°21′11″.06	26.56	25.28	25.51	24.63	24.62	-10.91	6.68
SCABS132739-412901	ESO324-024	$13^h27^m38^s.55$	-41°29′00″.93	26.10	24.91	25.27	24.38	24.19	-14.02	8.03
SCABS132745-420614	——	$13^h27^m44^s.81$	-42°06′13″.51	26.16	25.37	25.53	24.31	24.47	-8.84	5.87
SCABS132804-420834	——	$13^h28^m04^s.40$	-42°08′34″.36	26.46	24.88	25.00	23.91	23.92	-9.56	6.27
SCABS132835-415414	——	$13^h28^m34^s.80$	-41°54′13″.70	25.79	24.74	24.87	24.08	24.25	-10.03	6.29
SCABS132850-420504	——	$13^h28^m50^s.45$	-42°05′04″.26	27.59	25.89	26.35	24.99	25.12	-9.31	6.05
SCABS132910-451031	dw1329-45	$13^h29^m10^s.00$	-45°10′31″.00	28.85	27.23	27.52	26.74	25.70	-8.56	6.11
SCABS132916-450607	——	$13^h29^m15^s.89$	-45°06′06″.83	24.82	23.53	23.69	22.73	22.72	-11.42	7.06
SCABS132927-435740	——	$13^h29^m27^s.05$	-43°57′40″.01	25.77	24.31	24.39	23.35	23.45	-11.63	7.18
SCABS132957-415223	CenA-MM-Dw2	$13^h29^m57^s.34$	-41°52′22″.60	—	—	—	—	—	—	—
SCABS133014-415336	CenA-MM-Dw1	$13^h30^m14^s.26$	-41°53′35″.80	30.04	27.33	27.48	26.35	26.67	-10.69	7.53
SCABS133021-421133	CenA-MM-Dw3	$13^h30^m21^s.50$	-42°11′33″.00	—	—	—	—	—	—	—
SCABS133032-442318	——	$13^h30^m31^s.91$	-44°23′17″.91	28.95	27.42	27.28	26.52	26.89	-10.41	6.39

CONTINUED ON NEXT PAGE

Table B.1 – continued from previous page

ID	REFERENCE	α	δ	μ_u	μ_g	μ_r	μ_i	μ_z	M_V	LOG $\mathcal{M}_*$
SCABS133035-442641	——	$13^h30^m34^s.65$	-44°26′40″.88	28.16	26.65	26.57	26.00	26.58	-10.42	6.13
SCABS133042-444101	——	$13^h30^m42^s.29$	-44°41′00″.77	27.94	26.90	26.87	26.13	25.98	-7.19	5.80
SCABS133120-423211	——	$13^h31^m20^s.10$	-42°32′11″.30	26.51	25.22	25.59	24.25	24.19	-9.49	6.30
SCABS133141-435026	——	$13^h31^m41^s.06$	-43°50′25″.61	27.20	25.44	25.74	24.28	24.38	-9.46	6.17
SCABS133145-423038	——	$13^h31^m45^s.50$	-42°30′38″.00	26.29	25.30	25.97	24.54	24.63	-9.70	5.84
SCABS133151-441824	——	$13^h31^m50^s.80$	-44°18′23″.90	29.59	27.90	27.87	27.27	27.55	-9.27	5.65
SCABS133214-431727	——	$13^h32^m13^s.64$	-43°17′27″.10	25.56	24.33	24.43	23.35	23.47	-9.15	6.24
SCABS133301-410903	——	$13^h33^m01^s.40$	-41°09′02″.70	25.58	24.20	24.24	23.24	23.33	-9.79	6.64
SCABS133302-423148	CenA-MM-Dw9	$13^h33^m01^s.50$	-42°31′48″.00	—	—	—	—	—	—	—
SCABS133307-425205	——	$13^h33^m06^s.98$	-42°52′04″.87	26.98	25.78	25.33	24.60	24.27	-8.50	6.27
SCABS133334-413628	CenA-MM-Dw8	$13^h33^m34^s.10$	-41°36′28″.00	28.90	27.44	27.54	26.94	27.32	-10.31	6.36
SCABS133503-415507	——	$13^h35^m03^s.07$	-41°55′07″.02	26.23	24.80	24.95	23.75	23.92	-10.56	6.58
SCABS133523-412043	——	$13^h35^m23^s.03$	-41°20′42″.53	27.08	25.41	25.75	24.74	24.19	-8.95	5.89
SCABS133538-422358	——	$13^h35^m38^s.00$	-42°23′57″.50	25.36	24.18	24.23	23.32	23.43	-8.99	6.21
SCABS133644-442650	dw1336-44	$13^h36^m44^s.00$	-44°26′50″.00	27.78	26.53	26.23	25.35	25.19	-8.17	5.82
SCABS133734-441307	dw1337-44	$13^h37^m34^s.00$	-44°13′07″.00	28.72	26.92	27.35	26.67	28.39	-7.49	4.93
SCABS133755-415411	dw1337-41	$13^h37^m55^s.00$	-41°54′11″.00	29.05	27.62	27.86	27.79	27.97	-8.81	5.29

Photometric parameters of Centaurus A's dwarfs calculated with *GALFIT*. Cols. (1) and (2) list the dwarf IDs, and reference name if available, followed by the right ascension and declination in Cols. (3) and (4). Cols. (5)-(9) list the surface-brightness of the dwarf in the u', g', r', i', and z' passbands, respectively. Finally, Col. (10) lists the absolute V-band magnitudes, and Col. (11) the estimated total stellar masses ($\mathcal{M}_*$, in $M_\odot$).

Table B.2: Structural parameters of Centaurus A's dwarfs

		u′				g′				r′				i′				z′				
ID	REFERENCE	r_e	n	ϵ	PA	r_e	n	ϵ	PA	r_e	n	ϵ	PA	r_e	n	ϵ	PA	r_e	n	ϵ	PA	r_e
SCABS131200-422827	——	0.086	0.83	0.54	174.69	0.095	0.75	0.53	174.94	0.101	0.79	0.54	174.97	0.099	0.71	0.54	173.81	0.093	0.65	0.50	173.19	0.095
SCABS131210-424649	T18-dw1312-4247	0.084	0.98	0.30	28.84	0.098	0.91	0.23	30.83	0.097	0.91	0.15	21.26	0.098	0.80	0.17	33.40	0.086	0.72	0.14	23.80	0.093
SCABS131210-424648	T18-dw1312-4247	0.084	0.98	0.30	28.84	0.098	0.91	0.23	30.83	0.097	0.91	0.15	21.18	0.098	0.80	0.17	33.39	0.086	0.72	0.14	23.79	0.093
SCABS131222-421842	T18-dw1312-4219	0.140	0.74	0.07	146.63	0.184	1.13	0.09	257.02	0.126	0.77	0.08	233.58	0.129	0.58	0.34	234.44	0.076	0.22	0.07	146.63	0.131
SCABS131230-420328	——	0.071	1.22	0.21	73.30	0.082	1.07	0.20	72.41	0.083	1.05	0.19	76.03	0.087	0.97	0.20	76.14	0.090	0.93	0.24	77.59	0.083
SCABS131243-424651	T18-dw1313-4247	0.088	1.02	0.23	152.95	0.079	0.85	0.25	216.26	0.081	0.99	0.36	219.40	0.081	0.87	0.36	214.17	0.071	0.94	0.24	215.64	0.080
SCABS131245-414956	KK189	0.268	0.66	0.09	117.70	0.272	0.73	0.09	145.66	0.250	0.65	0.16	135.32	0.236	0.62	0.14	136.49	0.236	0.60	0.12	138.52	0.253
SCABS131334-421110	T18-dw1314-4211	0.231	1.03	0.34	25.27	0.213	0.78	0.48	36.36	0.183	0.80	0.43	32.47	0.190	0.97	0.38	31.21	0.222	0.62	0.49	41.84	0.208
SCABS131336-421408	T18-dw1314-4214	0.170	1.09	0.17	291.49	0.146	0.78	0.26	268.31	0.150	0.74	0.27	264.64	0.147	0.79	0.23	268.89	0.127	0.56	0.27	264.61	0.148
SCABS131350-422432	——	0.082	1.10	0.11	71.96	0.084	0.94	0.17	69.73	0.081	1.04	0.17	68.87	0.080	1.02	0.17	56.26	0.072	0.93	0.10	58.25	0.080
SCABS131359-415806	——	0.116	0.78	0.36	55.23	0.103	0.75	0.32	56.57	0.101	0.86	0.31	56.69	0.094	0.80	0.31	55.58	0.091	0.78	0.31	55.93	0.101
SCABS131408-420410	T18-dw1314-4204	0.082	0.86	0.30	172.79	0.082	0.80	0.23	169.36	0.084	0.97	0.23	170.08	0.078	0.91	0.23	167.39	0.072	0.84	0.24	167.77	0.080
SCABS131422-423043	T18-dw1314-4230	0.095	0.57	0.44	119.67	0.105	0.83	0.37	117.82	0.119	0.85	0.37	117.96	0.104	0.67	0.39	116.31	0.118	1.01	0.38	115.37	0.108
SCABS131445-414228	T18-dw1315-4142	0.083	0.67	0.40	114.80	0.080	0.82	0.38	119.65	0.071	0.85	0.47	110.96	0.076	1.38	0.47	103.43	0.066	0.74	0.58	115.26	0.075
SCABS131503-423218	T18-dw1315-4232	0.129	1.32	0.26	181.97	0.128	1.01	0.42	169.98	0.133	1.34	0.34	168.96	0.157	1.23	0.42	174.40	0.140	1.06	0.43	170.10	0.138
SCABS131534-430927	T18-dw1316-4309	0.122	0.93	0.37	161.59	0.116	0.07	0.49	127.96	0.111	0.30	0.27	143.77	0.109	0.37	0.14	177.40	0.128	0.06	0.42	187.12	0.117
SCABS131545-434350	——	0.109	1.07	0.23	53.37	0.119	1.30	0.15	66.73	0.106	1.19	0.13	71.45	0.088	0.98	0.17	68.72	0.079	0.93	0.22	65.75	0.100
SCABS131642-422406	T18-dw1317-4224	0.186	1.16	0.08	50.59	0.181	1.30	0.14	56.23	0.167	1.49	0.03	54.22	0.136	1.37	0.04	71.96	0.112	1.30	0.06	34.16	0.156
SCABS131727-432210	——	0.096	0.72	0.17	29.13	0.114	0.89	0.23	72.21	0.097	0.74	0.15	51.07	0.104	0.89	0.21	47.74	0.089	0.72	0.16	61.03	0.100
SCABS131748-425540	T18-dw1318-4256	0.222	0.10	0.40	85.23	0.215	0.10	0.15	141.58	0.204	0.10	0.31	96.45	0.231	0.10	0.41	97.91	0.177	0.10	0.45	80.72	0.210
SCABS131806-423337	T18-dw1318-4234	0.431	0.86	0.32	144.50	0.286	0.29	0.23	143.08	0.279	0.39	0.12	244.67	0.271	0.10	0.10	93.99	0.300	0.10	0.27	120.70	0.313
SCABS131815-430639	——	0.174	0.84	0.35	148.00	0.160	0.73	0.31	146.30	0.164	0.82	0.33	148.70	0.159	0.81	0.34	149.08	0.160	0.79	0.34	147.46	0.163
SCABS131858-445341	dw1318-44	0.136	0.26	0.59	1.82	0.107	0.40	0.54	15.80	0.098	0.16	0.44	48.90	0.076	0.40	0.40	33.68	0.050	0.73	0.46	36.84	0.094
SCABS131902-434417	——	0.115	0.95	0.23	67.15	0.107	0.96	0.21	63.60	0.107	1.23	0.22	67.17	0.104	1.18	0.24	64.23	0.099	1.14	0.24	63.84	0.106
SCABS131902-430749	——	0.173	0.65	0.27	131.54	0.190	0.69	0.29	134.87	0.202	0.73	0.31	136.29	0.203	0.71	0.31	135.60	0.202	0.69	0.32	135.10	0.194

CONTINUED ON NEXT PAGE

Table B.2 – continued from previous page

		u′				g′				r′				i′				z′				
ID	REFERENCE	r_e	n	ϵ	PA	r_e	n	ϵ	PA	r_e	n	ϵ	PA	r_e	n	ϵ	PA	r_e	n	ϵ	PA	r_e
SCABS131905-432305	——	0.100	0.49	0.49	167.17	0.094	0.60	0.36	161.78	0.084	0.69	0.31	148.14	0.077	0.68	0.20	151.36	0.083	0.80	0.29	164.18	0.088
SCABS131921-420339	T18-dw1319-4203	0.084	0.42	0.26	70.98	0.091	0.50	0.26	64.47	0.087	0.55	0.26	66.44	0.089	0.57	0.26	67.47	0.092	0.57	0.32	65.50	0.089
SCABS131952-415937	CenA-MM-Dw5	—	—	—	—	—	—	—	—	—	—	—	—	—	—	—	—	—	—	—	—	—
SCABS132037-433556	——	0.121	1.15	0.18	181.24	0.107	0.97	0.19	177.56	0.109	1.02	0.25	179.89	0.116	1.03	0.22	175.70	0.114	1.03	0.31	175.91	0.113
SCABS132049-423553	——	0.103	0.71	0.06	143.36	0.097	0.77	0.03	168.47	0.091	1.00	0.00	161.15	0.088	1.04	0.00	99.03	0.082	1.05	0.04	160.54	0.092
SCABS132109-433619	——	0.108	0.85	0.41	36.23	0.085	0.71	0.29	22.44	0.094	0.64	0.42	35.21	0.097	0.36	0.40	26.99	0.084	0.55	0.37	37.31	0.094
SCABS132138-435424	——	0.094	0.66	0.18	124.73	0.104	0.50	0.38	164.56	0.084	0.59	0.27	153.47	0.093	0.76	0.31	169.65	0.090	0.75	0.35	158.55	0.093
SCABS132140-430457	CenA-MM-Dw11b	—	—	—	—	—	—	—	—	—	—	—	—	—	—	—	—	—	—	—	—	—
SCABS132156-401938	——	0.075	0.70	0.38	21.08	0.072	0.69	0.29	19.84	0.074	0.91	0.32	19.92	0.071	0.92	0.30	20.42	0.069	0.99	0.29	18.85	0.072
SCABS132202-423209	KK197	0.945	0.16	0.62	113.06	0.913	0.31	0.61	113.58	0.885	0.46	0.55	116.95	0.927	0.25	0.64	118.16	0.924	0.18	0.64	116.60	0.919
SCABS132207-403141	——	0.208	0.59	0.44	177.76	0.203	1.08	0.31	193.43	0.185	1.09	0.28	201.96	0.179	1.06	0.29	201.42	0.171	1.00	0.33	199.85	0.189
SCABS132210-433256	——	0.097	1.06	0.21	124.69	0.105	1.14	0.20	127.84	0.114	1.49	0.22	131.92	0.096	1.26	0.25	130.54	0.079	1.05	0.21	132.35	0.098
SCABS132212-424359	[KK2000]55	0.634	0.13	0.46	50.33	0.768	0.29	0.41	59.16	0.692	0.26	0.32	51.62	0.631	0.30	0.32	51.17	0.736	0.15	0.54	48.10	0.692
SCABS132213-401734	——	0.089	1.17	0.21	65.74	0.073	0.78	0.13	108.02	0.081	1.04	0.21	130.04	0.078	0.93	0.25	138.64	0.074	0.99	0.24	131.45	0.079
SCABS132237-403437	——	0.112	0.50	0.24	173.65	0.105	0.51	0.20	173.79	0.104	0.58	0.23	175.88	0.104	0.60	0.23	173.40	0.101	0.62	0.24	172.00	0.105
SCABS132245-413224	——	0.092	0.48	0.26	56.70	0.103	0.42	0.36	57.37	0.116	0.45	0.29	64.29	0.111	0.33	0.30	80.17	0.130	0.42	0.25	57.24	0.111
SCABS132303-414710	CenA-MM-Dw4	0.282	0.10	0.41	25.73	0.341	0.48	0.41	34.88	0.330	0.37	0.39	31.70	0.275	0.30	0.34	23.45	0.256	0.40	0.35	31.51	0.297
SCABS132311-430153	——	0.111	0.64	0.05	59.81	0.127	0.76	0.19	84.04	0.112	0.60	0.22	72.93	0.115	0.71	0.22	73.90	0.110	0.54	0.32	73.63	0.115
SCABS132337-404317	dw1323-40c	—	—	—	—	—	—	—	—	—	—	—	—	—	—	—	—	—	—	—	—	—
SCABS132345-433920	——	0.077	0.66	0.14	18.72	0.087	0.65	0.21	40.85	0.077	0.61	0.21	42.29	0.081	0.67	0.26	41.17	0.074	0.55	0.26	44.55	0.079
SCABS132355-405009	dw1323-40b	0.563	0.65	0.55	173.05	0.386	0.39	0.61	166.74	0.406	0.59	0.57	167.60	0.377	0.18	0.63	166.65	0.315	0.23	0.70	168.83	0.409
SCABS132411-420827	CenA-MM-Dw12b	0.168	0.69	0.23	170.66	0.153	1.00	0.34	180.14	0.136	0.80	0.34	189.95	0.137	0.62	0.36	175.68	0.113	0.51	0.30	174.72	0.141
SCABS132431-432816	——	0.063	0.50	0.08	206.71	0.059	0.43	0.16	170.07	0.092	1.34	0.23	208.90	0.048	0.58	0.20	212.10	0.035	0.31	0.08	262.59	0.059
SCABS132433-444407	CenA-MM-Dw10	—	—	—	—	—	—	—	—	—	—	—	—	—	—	—	—	—	—	—	—	—
SCABS132453-404535	dw1323-40	0.277	0.35	0.20	134.03	0.355	0.55	0.16	162.01	0.329	0.50	0.20	177.37	0.269	0.30	0.16	165.93	0.276	0.20	0.35	201.25	0.301

CONTINUED ON NEXT PAGE

Table B.2 – continued from previous page

		u′				g′				r′				i′				z′				
ID	REFERENCE	r_e	n	ϵ	PA	r_e	n	ϵ	PA	r_e	n	ϵ	PA	r_e	n	ϵ	PA	r_e	n	ϵ	PA	r_e
SCABS132456-434012	——	0.113	0.82	0.35	7.29	0.125	0.91	0.30	6.82	0.140	0.94	0.35	10.42	0.131	0.95	0.30	11.48	0.122	0.88	0.30	9.67	0.126
SCABS132456-422247	——	0.262	0.75	0.37	32.56	0.279	0.90	0.37	41.49	0.297	1.02	0.40	42.94	0.268	1.01	0.40	40.86	0.260	0.96	0.40	45.00	0.273
SCABS132517-421829	——	0.108	1.36	0.19	74.16	0.097	1.19	0.18	72.80	0.088	1.29	0.18	71.20	0.083	1.33	0.16	69.36	0.076	1.24	0.15	67.32	0.090
SCABS132540-404150	——	0.138	0.98	0.04	246.14	0.126	1.00	0.04	166.34	0.126	1.23	0.04	170.41	0.116	1.24	0.03	185.04	0.112	1.26	0.05	177.40	0.124
SCABS132558-410539	CenA-MM-Dw6	0.392	0.10	0.52	104.97	0.267	0.25	0.26	267.25	0.231	0.23	0.30	92.43	0.204	0.10	0.21	141.04	0.152	0.18	0.20	175.32	0.249
SCABS132611-441557	——	0.159	0.49	0.24	188.89	0.166	0.57	0.26	182.95	0.167	0.62	0.26	182.75	0.164	0.60	0.24	181.34	0.160	0.61	0.23	179.07	0.163
SCABS132629-433324	CenA-MM-Dw7	—	—	—	—	—	—	—	—	—	—	—	—	—	—	—	—	—	—	—	—	—
SCABS132631-405530	——	0.086	1.09	0.25	185.63	0.098	1.22	0.31	195.41	0.086	1.55	0.41	182.63	0.078	1.54	0.33	180.16	0.075	1.63	0.31	178.61	0.085
SCABS132649-430002	CenA-MM-Dw10b	0.120	0.21	0.47	241.54	0.120	0.49	0.38	181.72	0.114	0.49	0.13	146.38	0.096	0.23	0.26	193.34	0.105	0.14	0.07	195.75	0.111
SCABS132704-431951	——	0.179	0.60	0.53	2.28	0.191	0.73	0.52	3.34	0.193	0.79	0.52	3.22	0.185	0.74	0.51	2.76	0.173	0.75	0.50	3.70	0.184
SCABS132711-423024	——	1.197	0.10	0.66	44.92	1.289	0.10	0.72	44.93	1.205	0.13	0.71	45.51	1.108	0.13	0.70	46.49	1.080	0.10	0.73	44.47	1.176
SCABS132725-404911	——	0.094	0.58	0.20	164.83	0.097	0.99	0.15	202.03	0.071	1.06	0.17	200.20	0.063	1.05	0.20	201.30	0.050	0.75	0.26	249.51	0.075
SCABS132728-452111	KK203	0.297	0.96	0.13	175.31	0.268	0.68	0.12	159.45	0.289	0.70	0.16	151.04	0.271	0.60	0.18	144.20	0.251	0.52	0.17	147.14	0.275
SCABS132739-412901	ESO324-024	1.057	0.98	0.37	76.64	1.026	0.63	0.40	76.98	1.075	0.58	0.42	75.14	1.038	0.49	0.42	74.82	0.936	0.50	0.36	74.62	1.026
SCABS132745-420614	——	0.104	0.28	0.04	7.51	0.101	0.64	0.12	82.62	0.113	0.88	0.15	51.32	0.095	0.59	0.19	53.87	0.095	0.33	0.29	65.94	0.102
SCABS132804-420834	——	0.132	1.38	0.37	22.56	0.108	1.11	0.37	21.64	0.105	1.41	0.35	24.05	0.094	1.22	0.37	24.31	0.087	1.14	0.39	24.00	0.105
SCABS132835-415414	——	0.130	0.69	0.06	232.74	0.136	0.88	0.13	184.04	0.123	1.28	0.07	147.64	0.116	1.20	0.18	170.96	0.110	1.41	0.26	166.65	0.123
SCABS132850-420504	——	0.198	0.90	0.26	167.46	0.167	0.61	0.26	176.51	0.203	0.82	0.31	170.11	0.157	0.58	0.29	180.22	0.147	0.46	0.32	182.43	0.174
SCABS132910-451031	dw1329-45	0.315	0.17	0.61	70.11	0.250	0.24	0.45	73.95	0.286	0.38	0.52	66.90	0.294	0.35	0.59	58.75	0.208	0.56	0.24	56.90	0.271
SCABS132916-450607	——	0.148	0.95	0.11	160.67	0.143	0.96	0.07	183.47	0.137	1.27	0.08	173.68	0.128	1.22	0.13	172.59	0.120	1.37	0.11	168.55	0.135
SCABS132927-435740	——	0.267	0.98	0.33	145.62	0.224	0.89	0.33	149.89	0.226	0.98	0.33	152.72	0.205	0.97	0.32	152.69	0.208	0.96	0.34	153.37	0.226
SCABS132957-415223	CenA-MM-Dw2	—	—	—	—	—	—	—	—	—	—	—	—	—	—	—	—	—	—	—	—	—
SCABS133014-415336	CenA-MM-Dw1	0.822	0.10	0.51	46.35	0.787	0.24	0.31	43.90	0.773	0.14	0.35	36.38	0.777	0.30	0.27	75.28	0.772	0.11	0.37	53.42	0.786
SCABS133021-421133	CenA-MM-Dw3	—	—	—	—	—	—	—	—	—	—	—	—	—	—	—	—	—	—	—	—	—
SCABS133032-442318	——	0.731	0.30	0.73	159.84	0.646	0.24	0.72	161.52	0.615	0.31	0.69	159.28	0.571	0.25	0.70	159.56	0.619	0.20	0.77	163.32	0.636

CONTINUED ON NEXT PAGE

Table B.2 – continued from previous page

		u′				g′				r′				i′				z′				
ID	REFERENCE	r_e	n	ϵ	PA	r_e	n	ϵ	PA	r_e	n	ϵ	PA	r_e	n	ϵ	PA	r_e	n	ϵ	PA	r_e
SCABS133035-442641	——	0.500	0.53	0.02	176.07	0.443	0.52	0.10	210.68	0.391	0.46	0.07	237.85	0.371	0.33	0.26	210.03	0.419	0.21	0.49	220.46	0.425
SCABS133042-444101	——	0.115	0.59	0.36	146.93	0.096	0.40	0.40	158.31	0.110	0.64	0.41	145.20	0.140	0.49	0.50	130.01	0.097	0.40	0.40	144.40	0.112
SCABS133120-423211	——	0.118	0.90	0.28	258.33	0.129	1.18	0.21	255.06	0.123	1.63	0.25	256.95	0.100	1.44	0.17	267.46	0.088	1.48	0.13	270.81	0.112
SCABS133141-435026	——	0.184	1.18	0.30	106.14	0.140	0.91	0.24	104.59	0.142	1.34	0.20	111.62	0.106	1.06	0.19	105.83	0.106	1.07	0.23	109.76	0.136
SCABS133145-423038	——	0.146	0.94	0.38	4.30	0.129	0.88	0.42	8.86	0.188	1.58	0.48	11.24	0.113	1.02	0.46	11.60	0.110	0.88	0.52	14.56	0.137
SCABS133151-441824	——	0.547	0.20	0.83	7.92	0.437	0.42	0.75	10.42	0.436	0.55	0.75	13.33	0.351	0.53	0.77	10.99	0.277	1.29	0.74	15.10	0.409
SCABS133214-431727	——	0.070	0.88	0.11	36.37	0.071	0.89	0.04	11.77	0.071	1.14	0.11	14.86	0.065	1.10	0.05	24.12	0.064	1.13	0.07	22.80	0.069
SCABS133301-410903	——	0.102	0.53	0.30	118.52	0.096	0.72	0.25	121.58	0.092	0.86	0.27	120.42	0.090	0.92	0.25	123.42	0.085	0.85	0.31	120.42	0.093
SCABS133302-423148	CenA-MM-Dw9	—	—	—	—	—	—	—	—	—	—	—	—	—	—	—	—	—	—	—	—	—
SCABS133307-425205	——	0.091	0.77	0.37	159.31	0.108	0.71	0.41	140.86	0.087	0.78	0.17	146.19	0.098	0.92	0.26	154.41	0.084	0.72	0.22	148.57	0.094
SCABS133334-413628	CenA-MM-Dw8	0.790	0.12	0.46	14.83	0.706	0.10	0.40	14.18	0.706	0.10	0.42	21.23	0.708	0.10	0.45	15.96	0.710	0.10	0.45	18.29	0.724
SCABS133503-415507	——	0.193	1.26	0.13	137.41	0.165	1.31	0.08	138.27	0.156	1.53	0.09	140.44	0.127	1.36	0.10	143.65	0.131	1.44	0.11	136.82	0.155
SCABS133523-412043	——	0.154	0.89	0.39	162.84	0.115	0.84	0.26	169.44	0.121	0.90	0.29	176.05	0.110	0.64	0.23	170.15	0.074	1.01	0.09	153.82	0.115
SCABS133538-422358	——	0.065	0.76	0.11	183.77	0.066	0.78	0.07	168.15	0.062	0.90	0.04	182.47	0.063	0.85	0.06	199.74	0.061	0.88	0.03	209.09	0.063
SCABS133644-442650	dw1336-44	0.180	0.33	0.18	16.25	0.157	0.10	0.37	97.07	0.146	0.22	0.20	93.88	0.137	0.26	0.21	81.50	0.144	0.10	0.15	94.03	0.153
SCABS133734-441307	dw1337-44	0.168	0.10	0.21	266.97	0.141	0.17	0.06	208.27	0.152	0.50	0.32	99.95	0.153	0.10	0.41	215.54	0.138	0.10	0.41	212.75	0.150
SCABS133755-415411	dw1337-41	0.386	0.10	0.67	24.37	0.383	0.16	0.52	22.24	0.398	0.11	0.57	26.21	0.342	0.10	0.60	20.64	0.357	0.10	0.61	25.04	0.373

Structural parameters of Centaurus A's dwarfs calculated with *GALFIT*. Cols. (1) and (2) list the dwarf IDs, and reference name if available. Cols. (3)-(22) list the effective radius (r_e, in kpc), Sérsic index (n), ellipticity (ϵ), and position angle (PA), in the u', g', r', i', and z' passbands, respectively. Finally, Col. (23) lists the total effective radius (r_e, in kpc).

[1] S. M. K. Alam, J. S. Bullock, and D. H. Weinberg. "Dark Matter Properties and Halo Central Densities." In: *ApJ* 572 (June 2002), pp. 34–40. DOI: 10.1086/340190.

[2] K. Bechtol et al. "Eight New Milky Way Companions Discovered in First-year Dark Energy Survey Data." In: *ApJ* 807, 50 (July 2015), p. 50. DOI: 10.1088/0004-637X/807/1/50. arXiv: 1503.02584.

[3] E. F. Bell, D. H. McIntosh, N. Katz, and M. D. Weinberg. "The Optical and Near-Infrared Properties of Galaxies. I. Luminosity and Stellar Mass Functions." In: *ApJS* 149 (Dec. 2003), pp. 289–312. DOI: 10.1086/378847. eprint: astro-ph/0302543.

[4] V. Belokurov et al. "Big Fish, Little Fish: Two New Ultra-faint Satellites of the Milky Way." In: *ApJ* 712 (Mar. 2010), pp. L103–L106. DOI: 10.1088/2041-8205/712/1/L103. arXiv: 1002.0504.

[5] P. Bennet, D. J. Sand, D. Crnojević, K. Spekkens, D. Zaritsky, and A. Karunakaran. "Discovery of Diffuse Dwarf Galaxy Candidates around M101." In: *ApJ* 850, 109 (Nov. 2017), p. 109. DOI: 10.3847/1538-4357/aa9180. arXiv: 1710.01728.

[6] E. Bertin. "Automatic Astrometric and Photometric Calibration with SCAMP." In: *Astronomical Data Analysis Software and Systems XV*. Ed. by C. Gabriel, C. Arviset, D. Ponz, and S. Enrique. Vol. 351. Astronomical Society of the Pacific Conference Series. July 2006, p. 112.

[7] E. Bertin and S. Arnouts. "SExtractor: Software for source extraction." In: *A&AS* 117 (June 1996), pp. 393–404. DOI: 10.1051/aas:1996164.

[8] E. Bertin, Y. Mellier, M. Radovich, G. Missonnier, P. Didelon, and B. Morin. "The TERAPIX Pipeline." In: *Astronomical Data Analysis Software and Systems XI*. Ed. by D. A. Bohlender, D. Durand, and T. H. Handley. Vol. 281. Astronomical Society of the Pacific Conference Series. 2002, p. 228.

[9] M. Boylan-Kolchin, J. S. Bullock, and M. Kaplinghat. "Too big to fail? The puzzling darkness of massive Milky Way subhaloes." In: *MNRAS* 415 (July 2011), pp. L40–L44. DOI: 10.1111/j.1745-3933.2011.01074.x. arXiv: 1103.0007 [astro-ph.CO].

[10] G. Bruzual and S. Charlot. "Stellar population synthesis at the resolution of 2003." In: *MNRAS* 344 (Oct. 2003), pp. 1000–1028. DOI: 10.1046/j.1365-8711.2003.06897.x. eprint: astro-ph/0309134.

[11] J. S. Bullock, A. V. Kravtsov, and D. H. Weinberg. "Hierarchical Galaxy Formation and Substructure in the Galaxy's Stellar Halo." In: *ApJ* 548 (Feb. 2001), pp. 33–46. DOI: 10.1086/318681. eprint: astro-ph/0007295.

[12] K. Chiboucas, I. D. Karachentsev, and R. B. Tully. "Discovery of New Dwarf Galaxies in the M81 Group." In: *AJ* 137 (Feb. 2009), pp. 3009–3037. DOI: 10.1088/0004-6256/137/2/3009. arXiv: 0805.1250.

[13] Chies-Santos, A. L., Cortesi, A., Fantin, D. S. M., Merrifield, M. R., Bamford, S., and Serra, P. "The nature of faint fuzzies from the kinematics of NGC3." In: *A&A* 559 (2013), A67. DOI: 10.1051/0004-6361/201322556. URL: https://doi.org/10.1051/0004-6361/201322556.

[14] L. Ciotti and G. Bertin. "Analytical properties of the $R^{1/m}$ law." In: *A&A* 352 (Dec. 1999), pp. 447–451. eprint: astro-ph/9911078.

[15] D. Crnojević, D. J. Sand, N. Caldwell, P. Guhathakurta, B. McLeod, A. Seth, J. D. Simon, J. Strader, and E. Toloba. "Discovery of a Close Pair of Faint Dwarf Galaxies in the Halo of Centaurus A." In: *ApJ* 795, L35 (Nov. 2014), p. L35. DOI: 10.1088/2041-8205/795/2/L35. arXiv: 1409.4776.

[16] D. Crnojević, D. J. Sand, K. Spekkens, N. Caldwell, P. Guhathakurta, B. McLeod, A. Seth, J. D. Simon, J. Strader, and E. Toloba. "The Extended Halo of Centaurus A: Uncovering Satellites, Streams, and Substructures." In: *ApJ* 823, 19 (May 2016), p. 19. DOI: 10.3847/0004-637X/823/1/19. arXiv: 1512.05366.

[17] D. Crnojević et al. "The Faint End of the Centaurus A Satellite Luminosity Function." In: *ApJ* 872, 80 (Feb. 2019), p. 80. DOI: 10.3847/1538-4357/aafbe7. arXiv: 1809.05103.

[18] P. Eigenthaler et al. "The Next Generation Fornax Survey (NGFS). II. The Central Dwarf Galaxy Population." In: *ApJ* 855, 142 (Mar. 2018), p. 142. DOI: 10.3847/1538-4357/aaab60. arXiv: 1801.02633.

[19] B. Flaugher et al. "The Dark Energy Camera." In: *AJ* 150, 150 (Nov. 2015), p. 150. DOI: 10.1088/0004-6256/150/5/150. arXiv: 1504.02900 [astro-ph.IM].

[20] G. L. H. Harris, M. Rejkuba, and W. E. Harris. "The Distance to NGC 5128 (Centaurus A)." In: *PASA* 27 (Oct. 2010), pp. 457–462. DOI: 10.1071/AS09061. arXiv: 0911.3180.

[21] C. Henkel, B. Javanmardi, D. Martínez-Delgado, P. Kroupa, and K. Teuwen. "DGSAT: Dwarf Galaxy Survey with Amateur Telescopes. II. A catalogue of isolated nearby edge-on disk galaxies and the discovery of new low surface brightness systems." In: *A&A* 603, A18 (July 2017), A18. DOI: 10.1051/0004-6361/201730539. arXiv: 1703.05356.

[22] B. Javanmardi, D. Martinez-Delgado, P. Kroupa, C. Henkel, K. Crawford, K. Teuwen, R. J. Gabany, M. Hanson, T. S. Chonis, and F. Neyer. "DGSAT: Dwarf Galaxy Survey with Amateur Telescopes. I. Discovery of low surface brightness systems around nearby spiral galaxies." In: *A&A* 588, A89 (Apr. 2016), A89. DOI: 10.1051/0004-6361/201527745. arXiv: 1511.04446.

[23] A. Jenkins, C. S. Frenk, S. D. M. White, J. M. Colberg, S. Cole, A. E. Evrard, H. M. P. Couchman, and N. Yoshida. "The mass function of dark matter haloes." In: *MNRAS* 321 (Feb. 2001), pp. 372–384. DOI: 10.1046/j.1365-8711.2001.04029.x. eprint: astro-ph/0005260.

[24] S. Jester et al. "The Sloan Digital Sky Survey View of the Palomar-Green Bright Quasar Survey." In: *AJ* 130 (Sept. 2005), pp. 873–895. DOI: 10.1086/432466. eprint: astro-ph/0506022.

[25] I. D. Karachentsev, D. I. Makarov, and E. I. Kaisina. "Updated Nearby Galaxy Catalog." In: *AJ* 145, 101 (Apr. 2013), p. 101. DOI: 10.1088/0004-6256/145/4/101. arXiv: 1303.5328 [astro-ph.CO].

[26] V. E. Karachentseva and I. D. Karachentsev. "A list of new nearby dwarf galaxy candidates." In: *A&AS* 127 (Feb. 1998), pp. 409–419. DOI: 10.1051/aas:1998109.

[27] V. E. Karachentseva and I. D. Karachentsev. "Southern Isolated Galaxy Triplets." In: *Astronomy Reports* 44 (Aug. 2000), pp. 501–522. DOI: 10.1134/1.1306352.

[28] E. N. Kirby, J. G. Cohen, P. Guhathakurta, L. Cheng, J. S. Bullock, and A. Gallazzi. "The Universal Stellar Mass-Stellar Metallicity Relation for Dwarf Galaxies." In: *ApJ* 779, 102 (Dec. 2013), p. 102. DOI: 10.1088/0004-637X/779/2/102. arXiv: 1310.0814 [astro-ph.GA].

[29] K. H. Knuth. "Optimal Data-Based Binning for Histograms." In: *arXiv Physics e-prints* (May 2006). eprint: physics/0605197.

[30] P. Kroupa, C. Theis, and C. M. Boily. "The great disk of Milky-Way satellites and cosmological sub-structures." In: *A&A* 431 (Feb. 2005), pp. 517–521. DOI: 10.1051/0004-6361:20041122. eprint: astro-ph/0410421.

[31] W. E. Kunkel and S. Demers. "The Magellanic Plane." In: *The Galaxy and the Local Group*. Ed. by R. J. Dickens, J. E. Perry, F. G. Smith, and I. R. King. Vol. 182. Royal Greenwich Observatory Bulletins. 1976, p. 241.

[32] A. Lauberts and E. A. Valentijn. *The surface photometry catalogue of the ESO-Uppsala galaxies*. 1989.

[33] D. Lynden-Bell. "Dwarf galaxies and globular clusters in high velocity hydrogen streams." In: *MNRAS* 174 (Mar. 1976), pp. 695–710. DOI: 10.1093/mnras/174.3.695.

[34] X. Ma, P. F. Hopkins, C.-A. Faucher-Giguère, N. Zolman, A. L. Muratov, D. Kereš, and E. Quataert. "The origin and evolution of the galaxy mass-metallicity relation." In: *MNRAS* 456 (Feb. 2016), pp. 2140–2156. DOI: 10.1093/mnras/stv2659. arXiv: 1504.02097.

[35] L. A. MacArthur, S. Courteau, and J. A. Holtzman. "Structure of Disk-dominated Galaxies. I. Bulge/Disk Parameters, Simulations, and Secular Evolution." In: *ApJ* 582 (Jan. 2003), pp. 689–722. DOI: 10.1086/344506. eprint: astro-ph/0208404.

[36] A. W. McConnachie. "The Observed Properties of Dwarf Galaxies in and around the Local Group." In: *AJ* 144, 4 (July 2012), p. 4. DOI: 10.1088/0004-6256/144/1/4. arXiv: 1204.1562.

[37] S. S. McGaugh, V. C. Rubin, and W. J. G. de Blok. "High-Resolution Rotation Curves of Low Surface Brightness Galaxies. I. Data." In: *AJ* 122 (Nov. 2001), pp. 2381–2395. DOI: 10.1086/323448. eprint: astro-ph/0107326.

[38] A. Merritt, P. van Dokkum, and R. Abraham. "The Discovery of Seven Extremely Low Surface Brightness Galaxies in the Field of the Nearby Spiral Galaxy M101." In: *ApJ* 787, L37 (June 2014), p. L37. DOI: 10.1088/2041-8205/787/2/L37. arXiv: 1406.2315.

[39] B. Moore, T. Quinn, F. Governato, J. Stadel, and G. Lake. "Cold collapse and the core catastrophe." In: *MNRAS* 310 (Dec. 1999), pp. 1147–1152. DOI: 10.1046/j.1365-8711.1999.03039.x. eprint: astro-ph/9903164.

[40] B. Moore, S. Ghigna, F. Governato, G. Lake, T. Quinn, J. Stadel, and P. Tozzi. "Dark Matter Substructure within Galactic Halos." In: *ApJ* 524 (Oct. 1999), pp. L19–L22. DOI: 10.1086/312287. eprint: astro-ph/9907411.

[41] R. P. Muñoz et al. "Unveiling a Rich System of Faint Dwarf Galaxies in the Next Generation Fornax Survey." In: *ApJ* 813, L15 (Nov. 2015), p. L15. DOI: 10.1088/2041-8205/813/1/L15. arXiv: 1510.02475.

[42] R. R. Muñoz, P. Côté, F. A. Santana, M. Geha, J. D. Simon, G. A. Oyarzún, P. B. Stetson, and S. G. Djorgovski. "A MegaCam Survey of Outer Halo Satellites. I. Description of the Survey." In: *ApJ* 860, 65 (June 2018), p. 65. DOI: 10.3847/1538-4357/aac168.

[43] R. R. Muñoz, P. Côté, F. A. Santana, M. Geha, J. D. Simon, G. A. Oyarzún, P. B. Stetson, and S. G. Djorgovski. "A MegaCam Survey of Outer Halo Satellites. III. Photometric and Structural Parameters." In: *ApJ* 860, 66 (June 2018), p. 66. DOI: 10.3847/1538-4357/aac16b.

[44] O. Müller, H. Jerjen, and B. Binggeli. "New low surface brightness dwarf galaxies in the Centaurus group." In: *A&A* 597, A7 (Jan. 2017), A7. DOI: 10.1051/0004-6361/201628921. arXiv: 1605.04130.

[45] O. Müller, H. Jerjen, and B. Binggeli. "The Leo-I group: new dwarf galaxy and ultra diffuse galaxy candidates." In: *A&A* 615, A105 (July 2018), A105. DOI: 10.1051/0004-6361/201832897. arXiv: 1802.08657.

[46] O. Müller, R. Scalera, B. Binggeli, and H. Jerjen. "The M 101 group complex: new dwarf galaxy candidates and spatial structure." In: *A&A* 602, A119 (June 2017), A119. DOI: 10.1051/0004-6361/201730434. arXiv: 1701.03681.

[47] J. F. Navarro, A. Ludlow, V. Springel, J. Wang, M. Vogelsberger, S. D. M. White, A. Jenkins, C. S. Frenk, and A. Helmi. "The diversity and similarity of simulated cold dark matter haloes." In: *MNRAS* 402 (Feb. 2010), pp. 21–34. DOI: 10.1111/j.1365-2966.2009.15878.x. arXiv: 0810.1522.

[48] Y. Ordenes-Briceño et al. "The Next Generation Fornax Survey (NGFS). III. Revealing the Spatial Substructure of the Dwarf Galaxy Population Inside Half of Fornax's Virial Radius." In: *ApJ* 859, 52 (May 2018), p. 52. DOI: 10.3847/1538-4357/aaba70. arXiv: 1803.10784.

[49] Y. Ordenes-Briceño et al. "The Next Generation Fornax Survey (NGFS). IV. Mass and Age Bimodality of Nuclear Clusters in the Fornax Core Region." In: *ApJ* 860, 4 (June 2018), p. 4. DOI: 10.3847/1538-4357/aac1b8. arXiv: 1805.00491.

[50] M. S. Pawlowski and P. Kroupa. "The rotationally stabilized VPOS and predicted proper motions of the Milky Way satellite galaxies." In: *MNRAS* 435 (Nov. 2013), pp. 2116–2131. DOI: 10.1093/mnras/stt1429. arXiv: 1309.1159.

[51] M. S. Pawlowski, B. Famaey, D. Merritt, and P. Kroupa. "On the Persistence of Two Small-scale Problems in ΛCDM." In: *ApJ* 815, 19 (Dec. 2015), p. 19. DOI: 10.1088/0004-637X/815/1/19. arXiv: 1510.08060.

[52] Planck Collaboration et al. "Planck 2015 results. XIII. Cosmological parameters." In: *A&A* 594, A13 (Sept. 2016), A13. DOI: 10.1051/0004-6361/201525830. arXiv: 1502.01589.

[53] R. Sánchez-Janssen et al. "The Next Generation Virgo Cluster Survey. VII. The Intrinsic Shapes of Low-luminosity Galaxies in the Core of the Virgo Cluster, and a Comparison with the Local Group." In: *ApJ* 820, 69 (Mar. 2016), p. 69. DOI: 10.3847/0004-637X/820/1/69. arXiv: 1602.00012.

[54] J. Schaye et al. "The EAGLE project: simulating the evolution and assembly of galaxies and their environments." In: *MNRAS* 446 (Jan. 2015), pp. 521–554. DOI: 10.1093/mnras/stu2058. arXiv: 1407.7040.

[55] E. F. Schlafly and D. P. Finkbeiner. "Measuring Reddening with Sloan Digital Sky Survey Stellar Spectra and Recalibrating SFD." In: *ApJ* 737, 103 (Aug. 2011), p. 103. DOI: 10.1088/0004-637X/737/2/103. arXiv: 1012.4804 [astro-ph.GA].

[56] M. F. Skrutskie et al. "The Two Micron All Sky Survey (2MASS)." In: *AJ* 131 (Feb. 2006), pp. 1163–1183. DOI: 10.1086/498708.

[57] V. Springel, J. Wang, M. Vogelsberger, A. Ludlow, A. Jenkins, A. Helmi, J. F. Navarro, C. S. Frenk, and S. D. M. White. "The Aquarius Project: the subhaloes of galactic haloes." In: *MNRAS* 391 (Dec. 2008), pp. 1685–1711. DOI: 10.1111/j.1365-2966.2008.14066.x. arXiv: 0809.0898.

[58] M. A. Taylor, R. P. Muñoz, T. H. Puzia, S. Mieske, P. Eigenthaler, and M. S. Bovill. "The Survey of Centaurus A's Baryonic Structures (SCABS). I. Survey Description and Initial Source Catalogues." In: *arXiv e-prints* (Aug. 2016). arXiv: 1608.07285.

[59] M. A. Taylor, T. H. Puzia, R. P. Muñoz, S. Mieske, A. Lançon, H. Zhang, P. Eigenthaler, and M. S. Bovill. "The Survey of Centaurus A's Baryonic Structures (SCABS) - II. The extended globular cluster system of NGC 5128 and its nearby environment." In: *MNRAS* 469 (Aug. 2017), pp. 3444–3467. DOI: 10.1093/mnras/stx1021. arXiv: 1608.07288.

[60] M. A. Taylor, P. Eigenthaler, T. H. Puzia, R. P. Muñoz, K. X. Ribbeck, H.-X. Zhang, Y. Ordenes-Briceño, and M. S. Bovill. "A Collection of New Dwarf Galaxies in NGC 5128's Western Halo." In: *ApJ* 867, L15 (Nov. 2018), p. L15. DOI: 10.3847/2041-8213/aae88d. arXiv: 1810.07194.

[61] F. Valdes, R. Gruendl, and DES Project. "The DECam Community Pipeline." In: *Astronomical Data Analysis Software and Systems XXIII*. Ed. by N. Manset and P. Forshay. Vol. 485. Astronomical Society of the Pacific Conference Series. May 2014, p. 379.

[62] M. Vogelsberger, S. Genel, V. Springel, P. Torrey, D. Sijacki, D. Xu, G. Snyder, D. Nelson, and L. Hernquist. "Introducing the Illustris Project: simulating the coevolution of dark and visible matter in the Universe." In: *MNRAS* 444 (Oct. 2014), pp. 1518–1547. DOI: 10.1093/mnras/stu1536. arXiv: 1405.2921.

[63] C. N. A. Willmer. "The Absolute Magnitude of the Sun in Several Filters." In: *ApJS* 236, 47 (June 2018), p. 47. DOI: 10.3847/1538-4365/aabfdf. arXiv: 1804.07788 [astro-ph.SR].

[64] C. Wittmann, T. Lisker, A. Pasquali, M. Hilker, and E. K. Grebel. "Peculiar compact stellar systems in the Fornax cluster." In: *MNRAS* 459 (July 2016), pp. 4450–4466. DOI: 10.1093/mnras/stw827. arXiv: 1605.01261.

[65] H.-X. Zhang et al. “Stellar Population Properties of Ultracompact Dwarfs in M87: A Mass-Metallicity Correlation Connecting Low-metallicity Globular Clusters and Compact Ellipticals.” In: *ApJ* 858, 37 (May 2018), p. 37. DOI: 10.3847/1538-4357/aab88a. arXiv: 1803.07577.

[66] S. van den Bergh. “The local group of galaxies.” In: *A&A Rev.* 9 (1999), pp. 273–318. DOI: 10.1007/s001590050019.